magnetochemistry

MDPI

# Supplementary Materials: Near-infrared emissive cyanido-bridged {YbFe2} molecular nanomagnets sensitive to the nitrile solvents of crystallization

**Michal Liberka [1], Kseniia Boidachenko [1], Jakub J. Zakrzewski [1], Mikolaj Zychowicz [1], Junhao Wang [2], Shin-ichi Ohkoshi [2] and Szymon Chorazy [1,*]**

[1] Faculty of Chemistry, Jagiellonian University, Gronostajowa 2, 30-387 Krakow, Poland; michal.liberka@doctoral.uj.edu.pl (M.L.); kseniia.boidachenko@student.uj.edu.pl (K.B.); jakub.j.zakrzewski@doctoral.uj.edu.pl (J.J.Z.); mikolaj.zychowicz@doctoral.uj.edu.pl (M.Z.); chorazy@chemia.uj.edu.pl (S.C.)

[2] Department of Chemistry, School of Science, The University of Tokyo, 7-3-1 Hongo, Bunkyo-ku, Tokyo 113-0033, Japan; wang-jh@chem.s.u-tokyo.ac.jp (J.W.); ohkoshi@chem.s.u-tokyo.ac.jp (S..O.)

* Correspondence: chorazy@chemia.uj.edu.pl


| | |
|---|---|
| Results of SEM–EDXMA analysis of metal ions in **1·MeCN** and **1·MeCN@Lu**. (Table S1) | 3 |
| IR spectra of **1·MeCN**, **1·MeCN@Lu**, **1·PrCN**, **1·AcrCN**, and **1·MalCN**. (Figure S1 with the comment) | 4 |
| Thermogravimetric curves for **1·MeCN**, **1·PrCN**, **1·AcrCN**, and **1·MalCN**. (Figure S2) | 5 |
| Crystal data and structure refinement for **1·MeCN**, **1·PrCN**, **1·AcrCN**, and **1·MalCN**. (Table S2) | 6 |
| Detailed structure parameters of $Yb^{III}$ and $Fe^{II}$ complexes in **1·MeCN**, **1·PrCN**, **1·AcrCN**, and **1·MalCN**. (Tables S3–S6) | 7–10 |
| Comparison of the crystal structures of **1·MeCN**, **1·PrCN**, **1·AcrCN**, and **1·MalCN**. (Figure S3) | 11 |
| The views of the crystal structure of **1·MeCN** along three main crystallographic axes. (Figure S4) | 12 |
| The views of supramolecular interactions in the crystal structure of **1·MeCN** including the interactions between {$YbFe_2$} molecules and their interactions with solvent and anions. (Figure S5) | 13 |
| The views of the crystal structure of **1·AcrCN** along three main crystallographic axes. (Figure S6) | 14 |
| The views of supramolecular interactions in the crystal structure of **1·AcrCN** including the interactions between {$YbFe_2$} molecules and their interactions with solvent and anions. (Figure S7) | 15 |
| The views of the crystal structure of **1·PrCN** along three main crystallographic axes. (Figure S8) | 16 |
| The views of supramolecular interactions in the crystal structure of **1·PrCN** including the interactions between {$YbFe_2$} molecules and their interactions with solvent and anions. (Figure S9) | 17 |
| The views of the crystal structure of **1·PrCN** along three main crystallographic axes. (Figure S10) | 18 |
| The views of supramolecular interactions in the crystal structure of **1·MalCN** including the interactions between {$YbFe_2$} molecules and their interactions with solvent and anions. (Figure S11) | 19 |
| Results of Continuous Shape Measure analysis for Yb(III) and Fe(II) complexes in **1·MeCN**, **1·PrCN**, **1·AcrCN**, and **1·MalCN**. (Table S7) | 20 |
| The visualization of Yb···Yb distances in the crystal structures of **1·MeCN**, **1·PrCN**, **1·AcrCN**, and | 21 |

| | |
|---|---|
| **1·MalCN**. (Figure S12) | |
| Comparison of closest Yb···Yb distances in the crystal structures of **1·MeCN**, **1·PrCN**, **1·AcrCN**, and **1·MalCN**. (Table S8) | 22 |
| Powder X-ray diffraction (P-XRD) patterns of **1·MeCN**, **1·PrCN**, **1·AcrCN**, and **1·MalCN**. (Figure S13) | 23 |
| Experimental direct-current (*dc*) magnetic characteristics of **1·MeCN**, **1·MeCN@Lu**, **1·PrCN**, **1·AcrCN**, and **1·MalCN**, together with the comparison with the theoretical ones, obtained using the *ab initio* calculations for **1·MeCN**. (Figure S14) | 24 |
| Complete magnetic-field-variable (for $T$ = 1.8 K) and temperature-variable (for $H_{dc}$ of 800 Oe and 6000 Oe) alternate-current magnetic susceptibility characteristics for **1·MeCN**. (Figures S15–S16) | 25–26 |
| Complete magnetic-field-variable (for $T$ = 1.8 K) and temperature-variable (for $H_{dc}$ = 800 Oe) alternate-current magnetic susceptibility characteristics for **1·MeCN@Lu**. (Figures S17–S18) | 27–28 |
| Description of the basis sets (**1S** and **1L**) employed in the *ab initio* calculations of the $Yb^{III}$ crystal field in **1·MeCN**. (Table S9) | 29 |
| Summary of the energy splitting of the $^2F_{7/2}$ multiplet of $Yb^{III}$ in **1S** model with pseudo-*g*-tensors of each Kramers doublet. (Table S10) | 29 |
| Summary of the energy splitting of the $^2F_{7/2}$ multiplet of $Yb^{III}$ in **1L** model with pseudo-*g*-tensors of each Kramers doublet. (Table S11) | 30 |
| The energy splitting of the excited $^2F_{5/2}$ multiplet of $Yb^{III}$ complexes extracted from the *ab initio* calculations. (Table S12) | 30 |
| Comment to the *ab initio* calculations performed for **1·MeCN**. | 31 |
| Complete magnetic-field-variable (for $T$ = 1.8 K) and temperature-variable (for $H_{dc}$ = 800 Oe) *ac* magnetic characteristics of **1·AcrCN**. (Figure S19–S20) | 32–33 |
| Complete magnetic-field-variable (for $T$ = 1.8 K) and temperature-variable (for $H_{dc}$ = 800 Oe) *ac* magnetic characteristics of **1·PrCN**. (Figure S21–S22) | 34–35 |
| Complete magnetic-field-variable (for $T$ = 1.8 K) and temperature-variable (for $H_{dc}$ = 800 Oe) *ac* magnetic characteristics of **1·MalCN**. (Figure S23–S24) | 36–37 |
| Comment to Figures S15–S24. | 38 |
| Solid-state UV-vis-NIR absorption spectra of **1·MeCN**, **1·PrCN**, **1·AcrCN**, and **1·MalCN**. (Figure S25 with the comment). | 39 |
| Solid–state excitation and emission spectra of **1·MeCN**, **1·PrCN**, **1·AcrCN**, and **1·MalCN**, gathered at two different temperatures, 77 K and 290 K. (Figure S26) | 40 |
| References to Supporting Information. | 41 |

**Table S1.** Results of SEM–EDXMA analysis of metal ions in **1·MeCN** and **1·MeCN@Lu**.

| **metal** | **Fe** | **Yb** | **Lu** |
|---|---|---|---|
| compound | | **1·MeCN** | |
| measured atomic composition (only metals included, independent measurements)* / % | 17.89(0.36) | 8.26(0.50) | - |
| | 17.11(0.37) | 10.12(0.33) | - |
| | 16.58(0.58) | 9.01(0.56) | - |
| | 17.77(0.55) | 9.23(0.53) | - |
| | 17.22(0.43) | 8.14(0.52) | - |
| | 14.71(0.53) | 9.90(0.53) | - |
| | 18.17(0.58) | 8.97(0.53) | - |
| | 16.86(0.57) | 9.12(0.54) | - |
| average atomic composition (only metal included) / % | 17.04(0.50) | 9.09(0.51) | - |
| relative atomic composition (only metals included, calculated for two Fe centers) | 2 | 1.07(0.1) ≈ 1 | - |
| proposed composition | 2 | 1 | - |
| determined formula | | $\{Yb^{III}(4\text{-pyridone})_4[Fe^{II}(phen)_2(CN)_2]_2\}(CF_3SO_3)_3\cdot 2MeCN$ | |
| metal | Fe | Yb | Lu |
| compound | | **1·MeCN@Lu** | |
| measured atomic composition (only metals included, independent measurements)* / % | 12.76(0.48) | 0.57(0.21) | 6.69(0.31) |
| | 12.48(0.32) | 0.55(0.27) | 8.54(0.67) |
| | 17.08(0.37) | 0.58(0.28) | 8.07(0.69) |
| | 16.92(0.55) | 0.68(0.27) | 8.05(0.66) |
| | 17.67(0.63) | 0.67(0.30) | 8.73(0.74) |
| | 11.57(0.32) | 0.37(0.27) | 9.31(0.69) |
| | 16.49(0.57) | 0.90(0.24) | 8.05(0.35) |
| | 14.89(0.38) | 0.62(0.31) | 8.86(0.76) |
| average atomic composition (only metal included) / % | 14.98(0.45) | 0.62(0.27) | 8.29(0.76) |
| relative atomic composition (only metals included, calculated for two Fe centers) | 2 | 0.08(0.04) | 1.11(0.08) |
| | | 1.19(0.6) ≈ 1 | |
| lanthanides ratio | - | 0.07(0.04) [0.08/1.19] | 0.93(0.08) [1.11/1.19] |
| proposed composition | 2 | 0.07 | 0.93 |
| determined formula | | $\{Yb^{III}_{0.07}Lu^{III}_{0.93}(4\text{-pyridone})_4[Fe^{II}(phen)_2(CN)_2]_2\}(CF_3SO_3)_3\cdot 2MeCN$ | |

*For each compound, EDXMA (energy dispersive X-ray microanalysis) analyses were conducted on a few different single crystals and on a few places of the selected single crystal.

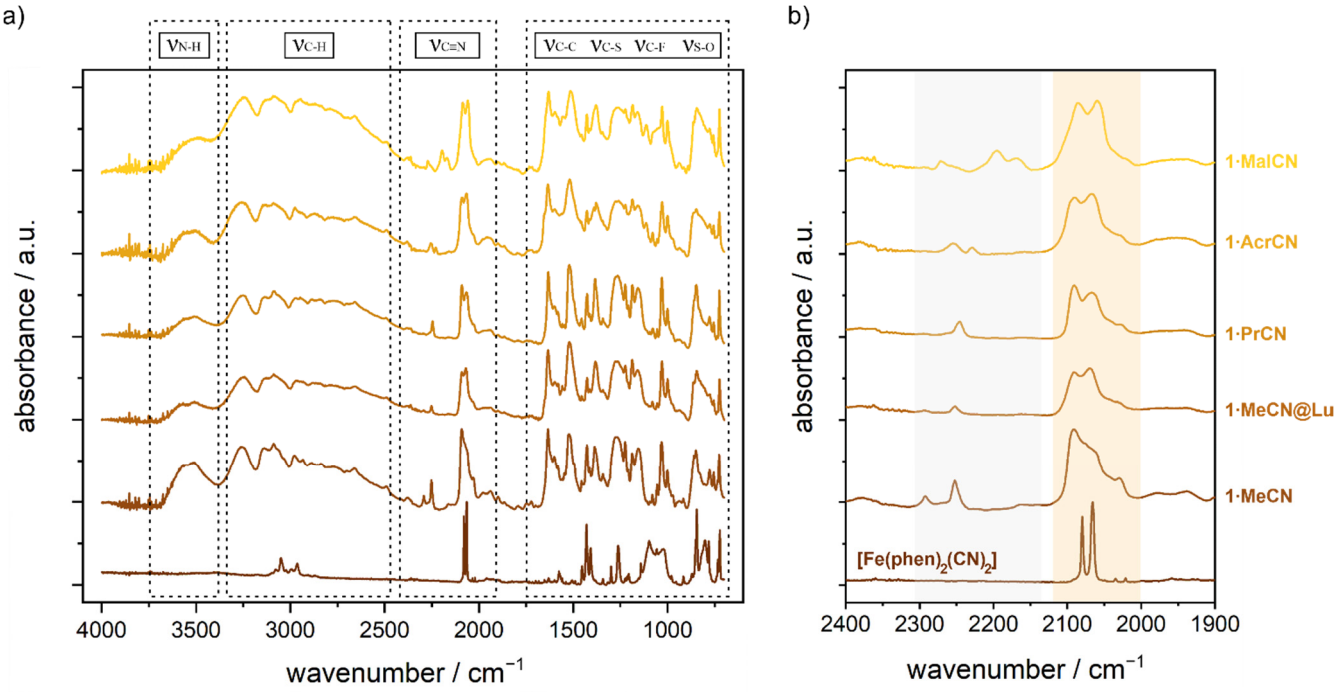


**Figure S1.** Infrared absorption spectra of the crystalline samples of **1·MeCN**, **1·MeCN@Lu**, **1·PrCN**, **1·AcrCN**, and **1·MalCN** presented in the broad 4000–700 $cm^{-1}$ (a) and the limited 2400–1900 $cm^{-1}$ ranges (b). The spectra were compared with $[Fe^{II}(phen)_2(CN)_2]\cdot 2H_2O$ precursor complex.

**Comment to Figure S1:**

The broad absorption above 2500 $cm^{-1}$ is related to the stretching vibrations, ν(C–H) and ν(N–H), of nitrile solvent molecules, 4-pyridone, and phen organic ligands. The 1750–700 $cm^{-1}$ range, consisting of a large number of absorption peaks, is related to the skeletal vibrations, ν(C–H), ν(C–C) and ν(C–N), of organic ligands, as well as stretching modes, ν(S–O), ν(S–C) and ν(C–F), of trifluoro-methanesulfonate anions [S1,S2]. In the 2400–1900 $cm^{-1}$ range, the characteristic peaks related to the stretching vibrations of C≡N groups are observed. The higher energy bands above 2150 $cm^{-1}$ can be assigned to the nitrile group of solvents molecules, while a set of lower energy peaks below 2150 $cm^{-1}$ is related to cyanido ligands. Comparing to the $[Fe^{II}(phen)_2(CN)_2]\cdot 2H_2O$ precursor, the cyanido ligand stretching vibrations in **1·MeCN**, **1·MeCN@Lu**, **1·PrCN**, **1·AcrCN**, and **1·MalCN** appear within a slightly broader range covered by a few overlapping peaks. This range can be divided into the part related to the terminal cyanido ligands, represented by IR peaks of the 2080–2010 $cm^{-1}$ range, and the higher energy part ascribable to the bridging -C≡N- groups, which is observed in 2140–2080 $cm^{-1}$ region in the presented compounds while being absent in iron(II)–cyanide precursor [S3]. This interpretation stays in good agreement with the structural data showing that $[Fe^{II}(phen)_2(CN)_2]$ complexes serve as metalloligands to $Yb^{III}$ metal centers (Figure 1).

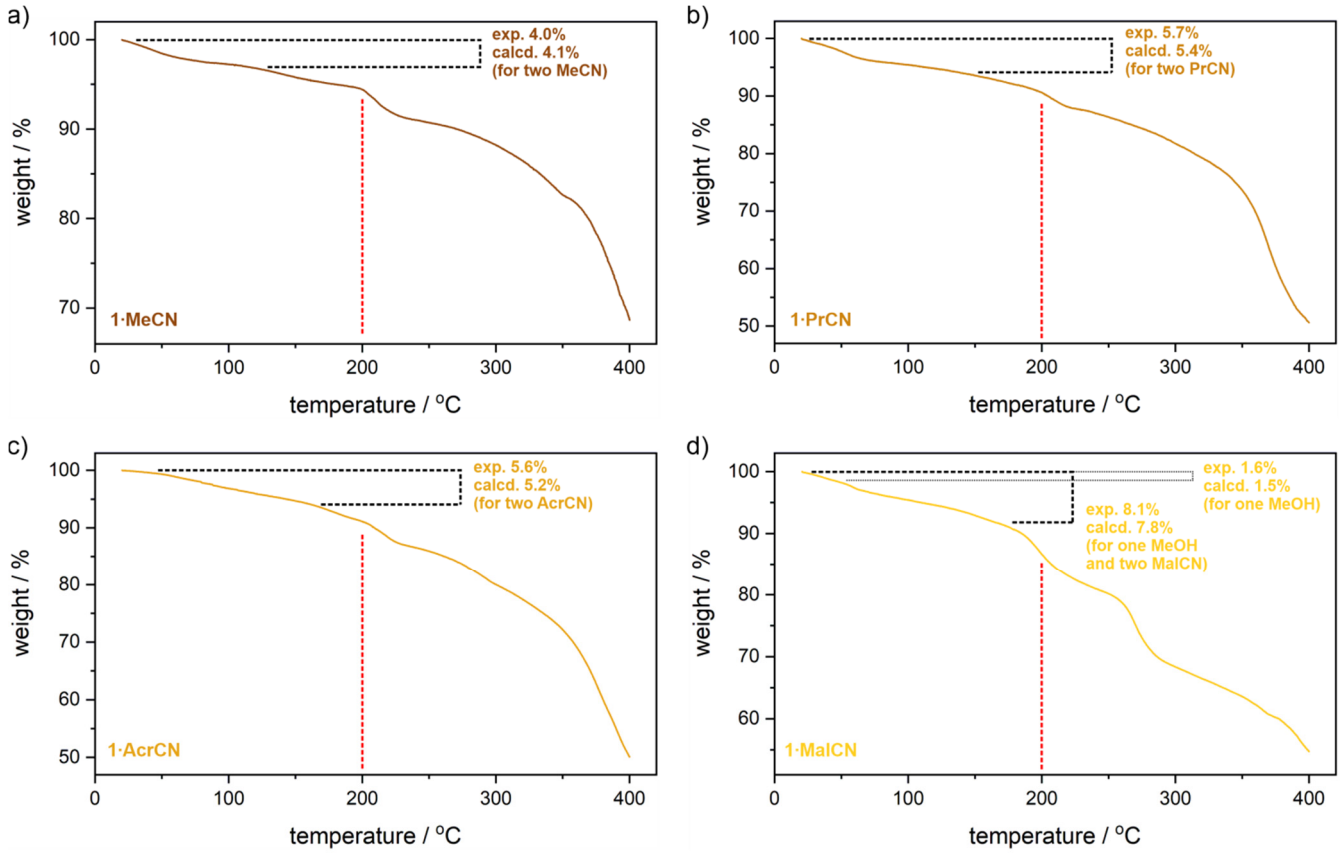


**Figure S2.** Thermogravimetric (TG) curves collected in the temperature range 20–400°C for the crystalline samples of **1·MeCN** (a), **1·PrCN** (b), **1·AcrCN** (c), and **1·MalCN** (d). The steps related to the loss of solvent molecules are depicted. The critical temperature of 200 °C, below which the presumable decomposition of the samples occurs, was emphasized by red dotted line.

**Comment to Figure S2:**

In all samples, **1·MeCN**, **1·PrCN**, **1·AcrCN**, and **1·MalCN**, the immediately mass decrease occurs after starting up to 150 °C. The initial mass decreases of 4.0%, 5.7%, and 5.6% in **1·MeCN**, **1·PrCN** and **1·AcrCN**, respectively, are related to the removal of two MeCN/PrCN/AcrCN crystallization solvent molecules per {YbFe$_2$} formula units. More complex behavior is observed in **1·MalCN**, where two subsequent steps, the first related to the removal of one MeOH and the second related to the removal of two MalCN molecules, are observed, giving the total decrease of 8.1% of the sample mass. The related experimental weight losses of all these steps are in line with the expected mass change deduced from the CHN elemental analysis (see the experimental section). After the initial decrease of the sample mass, further heating leads to the gradual considerable mass change which occurs significantly above 200°C, with the quite similar course in all samples. These changes presumably lead to the decomposition of the compounds. The complicated course of the TG curves, due to many indistinguishable changes, makes it difficult to interpret the results unambiguously. However, comparing with the literature data, it can be assumed that the high-temperature mass decreases are related to a series of successive changes within the anions, e.g. the formation of $CF_3SO_2^-$, $CF_3CO_3^-$ and/or $(CF_3CO_2)O$, their decomposition (e.g. to $CO_2$, CO, $CHF_3$, $F_2$, $SO_2$), and the removal of cyanido and organic ligands [S4,S5].

**Table S2.** Crystal data and structure refinement parameters for **1·MeCN**, **1·PrCN**, **1·AcrCN**, and **1·MalCN**.

| | **1·MeCN** | **1·AcrCN** | **1·PrCN** | **1·MalCN** |
|---|---|---|---|---|
| formula | $C_{79}H_{58}F_9Fe_2N_{18}O_{13}S_3Yb$ | $C_{81}H_{58}F_9Fe_2N_{18}O_{13}S_3Yb$ | $C_{81}H_{62}F_9Fe_2N_{18}O_{13}S_3Yb$ | $C_{164}H_{120}F_{18}Fe_4N_{40}O_{28}S_6Yb_2$ |
| formula weight / g·mol$^{-1}$ | 2019.35 | 2043.37 | 2047.4 | 4202.83 |
| crystal description | red needle | | | red plate |
| $T$ / K | 100(2) | | | |
| $\lambda$ / Å | 0.71073 (Mo K$\alpha$) | | | |
| crystal system | monoclinic | | | |
| space group | *C* 2/*c* | | | |
| $a$ / Å | 24.0591(18) | 24.3976(12) | 24.413(3) | 23.7146(9) |
| $b$ / Å | 21.8075(16) | 21.9482(11) | 21.988(2) | 21.4669(9) |
| $c$ / Å | 17.4040(13) | 17.3099(8) | 17.264(2) | 18.1322(7) |
| $\alpha$ / deg | 90 | 90 | 90 | 90 |
| $\beta$ / deg | 112.174(2) | 111.8610(10) | 112.169(3) | 108.7190(10) |
| $\gamma$ / deg | 90 | 90 | 90 | 90 |
| $V$ / Å$^3$ | 8456.0(11) | 8602.6(7) | 8582.2(17) | 8742.5(6) |
| $Z$ | 4 | 4 | 4 | 2 |
| calculated density / g·cm$^{-1}$ | 1.586 | 1.578 | 1.585 | 1.597 |
| absorption coefficinet / cm$^{-1}$ | 1.602 | 1.575 | 1.579 | 1.554 |
| $F$(000) | 4052 | 4100 | 4116 | 4220 |
| crystal size / mm×mm×mm | 0.14×0.12×0.05 | 0.14×0.1×0.07 | 0.2×0.08×0.07 | 0.42×0.12×0.11 |
| $\Theta$ range / ° | 2.499–25.027 | 2.247–25.027 | 2.248–25.027 | 2.238–25.027 |
| limiting indices | -28 < $h$ < 28<br>-25 < $k$ < 25<br>-20 < $l$ < 20 | -29 < $h$ < 29<br>-26 < $k$ < 26<br>-20 < $l$ < 20 | -29 < $h$ < 29<br>-26 < $k$ < 26<br>-20 < $l$ < 20 | -28 < $h$ < 28<br>-25 < $k$ < 25<br>-21 < $l$ < 21 |
| collected reflections | 38975 | 43384 | 47555 | 46012 |
| $R_{int}$ | 0.058 | 0.0761 | 0.0442 | 0.0866 |
| completeness | 0.999 | 0.999 | 0.999 | 0.999 |
| data/restraints/ parameters | 7469/193/601 | 7600/138/613 | 7579/182/610 | 7708/235/657 |
| GOF on $F^2$ | 1.038 | 1.055 | 1.099 | 1.098 |
| final $R$ indices | $R_1$ = 0.11 [$I$>2$\sigma$($I$)]<br>$wR_2$ = 0.336 (all) | $R_1$ = 0.099 [$I$>2$\sigma$($I$)]<br>$wR_2$ = 0.296 (all) | $R_1$ = 0.104 [$I$>2$\sigma$($I$)]<br>$wR_2$ = 0.289 (all) | $R_1$ = 0.098 [$I$>2$\sigma$($I$)]<br>$wR_2$ = 0.256 (all) |
| largest diffraction peak and hole / e·Å$^{-3}$ | 2.294 and -1.808 | 3.07 and -1.973 | 3.75 and -1.907 | 2.056 and -1.968 |

**Table S3.** Detailed structure parameters of $Yb^{III}$ and $Fe^{II}$ complexes in **1·MeCN**.

| **1·MeCN** | | | | | |
|---|---|---|---|---|---|
| **distances in ytterbium(III) and iron(II) complexes / Å** | | | | | |
| **Yb1-O1** | **2.141(13)** | **Fe1-C2** | **1.894(16)** | Fe1-N6 | 1.989(12) |
| Yb1-O2 | 2.217(10) | Fe1-N3 | 1.952(11) | C1≡N1 | 1.14(2) |
| Yb1-N1 | 2.334(14) | Fe1-N4 | 1.999(12) | C2≡N2 | 1.147(19) |
| Fe1-C1 | 1.885(18) | Fe1-N5 | 1.986(13) | Yb1-Fe1 | 5.276(9) |
| angles in ytterbium(III) and iron(II) complexes / deg | | | | | |
| O1-Yb1-O2 | 90.7(4)/ 89.3(4) | N4-Fe1-N5 | 91.0(5) | N5-Fe1-N6 | 80.8(5) |
| O1-Yb1-N1 | 90.5(5)/ 89.5(5) | N5-Fe1-C1 | 91.3(5) | N6-Fe1-C2 | 93.5(6) |
| O2-Yb1-N1 | 93.5(4)/ 86.5(4) | C1-Fe1-N3 | 94.1(6) | C1-Fe1-N4 | 175.9(5) |
| O1-Yb1-O1 | 180.0 | N3-Fe1-N4 | 82.4(5) | C2-Fe1-N5 | 174.3(5) |
| O2-Yb1-O2 | 180.00(14) | N4-Fe1-N6 | 92.1(5) | N3-Fe1-N6 | 170.0(5) |
| N1-Yb1-N1 | 180.0(7) | N6-Fe1-C1 | 91.6(6) | Yb1-C1≡N1 | 161.0(12) |
| C1-Fe1-C2 | 88.3(6) | C2-Fe1-N3 | 94.8(5) | - | - |
| C2-Fe1-N4 | 89.8(6) | N3-Fe1-N5 | 90.9(5) | - | - |
| details of crystallization solvent geometry / Å, deg | | | | | |
| N1S≡C1S | 1.11(3) | C1S-C2S | 1.38(4) | N1S≡C1S-C2S | 172(3) |

**Table S4.** Detailed structure parameters of $Yb^{III}$ and $Fe^{II}$ complexes in **1·AcrCN**.

| **1·AcrCN** | | | | | |
|---|---|---|---|---|---|
| **distances in ytterbium(III) and iron(II) complexes / Å** | | | | | |
| **Yb1-O1** | **2.138(19)/ 2.171(19)** | **Fe1-C2** | **1.911(14)** | Fe1-N6 | 1.970(9) |
| Yb1-O2 | 2.104(14)/ 2.304(13) | Fe1-N3 | 1.966(10) | C1≡N1 | 1.154(16) |
| Yb1-N1 | 2.194(14)/ 2.466(14) | Fe1-N4 | 2.005(11) | C2≡N2 | 1.141(16) |
| Fe1-C1 | 1.883(15) | Fe1-N5 | 1.991(11) | Yb1-Fe1 | 5.252(4) |
| angles in ytterbium(III) and iron(II) complexes / deg | | | | | |
| O1-Yb1-O2 | 92.8(7)/ 88.2(6) | N4-Fe1-N5 | 89.0(4) | N5-Fe1-N6 | 81.5(4) |
| O1-Yb1-N1 | 94.5(7)/ 92.5(6) | C1-Fe1-N4 | 91.8(4) | N6-Fe1-C2 | 94.3(4) |
| O2-Yb1-N1 | 94.0(5)/ 92.9(6) | C1-Fe1-N3 | 91.5(4) | C2-Fe1-N4 | 174.6(5) |
| O1-Yb1-O1 | 171.2(3) | N3-Fe1-N4 | 81.0(4) | N5-Fe1-C1 | 175.8(5) |
| O2-Yb1-O2 | 173.1(4) | N4-Fe1-N6 | 91.0(4) | N3-Fe1-N6 | 170.2(5) |
| N1-Yb1-N1 | 175.3(5) | N6-Fe1-C1 | 94.3(5) | Yb1-C1≡N1 | 155.5(10)/ 159.5(10) |
| C1-Fe1-C2 | 88.8(5) | C2-Fe1-N3 | 93.7(5) | - | - |
| C2-Fe1-N5 | 90.8(5) | N3-Fe1-N5 | 92.7(4) | - | - |
| details of crystallization solvent geometry / Å, deg | | | | | |
| N1S≡C1S | 1.13(2) | C2S-C3S | 1.14(3) | C1S-C2S-C3S | 120(3) |
| C1S-C2S | 1.45(3) | N1S≡C1S-C2S | 164(3) | | |

**Table S5.** Detailed structure parameters of $Yb^{III}$ and $Fe^{II}$ complexes in **1·PrCN**.

| **1·PrCN** | | | | | |
|---|---|---|---|---|---|
| **distances in ytterbium(III) and iron(II) complexes / Å** | | | | | |
| **Yb1-O1** | **2.194(10)** | **Fe1-C2** | **1.912(12)** | Fe1-N6 | 1.980(9) |
| Yb1-O2 | 2.142(10) | Fe1-N3 | 1.975(9) | C1≡N1 | 1.157(15) |
| Yb1-N1 | 2.314(10) | Fe1-N4 | 2.006(10) | C2≡N2 | 1.147(15) |
| Fe1-C1 | 1.896(12) | Fe1-N5 | 2.000(10) | Yb1-Fe1 | 5.257(3) |
| angles in ytterbium(III) and iron(II) complexes / deg | | | | | |
| O1-Yb1-O2 | 90.4(4)/ 89.6(4) | N4-Fe1-N5 | 89.7(4) | N5-Fe1-N6 | 82.0(4) |
| O1-Yb1-N1 | 92.7(4)/ 87.3(4) | C1-Fe1-N4 | 91.3(4) | N6-Fe1-C2 | 93.2(4) |
| O2-Yb1-N1 | 91.8(4)/ 88.2(4) | C1-Fe1-N3 | 91.6(4) | C2-Fe1-N4 | 175.8(4) |
| O1-Yb1-O1 | 180.0 | N3-Fe1-N4 | 82.1(4) | N5-Fe1-C1 | 175.5(4) |
| O2-Yb1-O2 | 180.0 | N4-Fe1-N6 | 90.9(4) | N3-Fe1-N6 | 171.4(4) |
| N1-Yb1-N1 | 180.0 | N6-Fe1-C1 | 93.6(4) | Yb1-C1≡N1 | 158.1(8) |
| C1-Fe1-C2 | 89.2(5) | C2-Fe1-N3 | 93.7(4) | - | - |
| C2-Fe1-N5 | 90.2(4) | N3-Fe1-N5 | 92.8(4) | - | - |
| details of crystallization solvent geometry / Å, deg | | | | | |
| N1S≡C1S | 1.06(2) | C2S-C3S | 1.36(4) | C1S-C2S-C3S | 120(3) |
| C1S-C2S | 1.41(4) | N1S≡C1S-C2S | 170(3) | | |

**Table S6.** Detailed structure parameters of $Yb^{III}$ and $Fe^{II}$ complexes in **1·MalCN**.

| **1·MalCN** | | | | | |
|---|---|---|---|---|---|
| distances in ytterbium(III) and iron(II) complexes / Å | | | | | |
| Yb1-O1 | 2.178(8) | Fe1-C2 | 1.907(15) | Fe1-N6 | 1.969(10) |
| Yb1-O2 | 2.197(8) | Fe1-N3 | 1.985(11) | C1≡N1 | 1.173(16) |
| Yb1-N1 | 2.340(10) | Fe1-N4 | 2.002(13) | C2≡N2 | 1.155(18) |
| Fe1-C1 | 1.871(11) | Fe1-N5 | 1.995(11) | Yb1-Fe1 | 5.328(6) |
| angles in ytterbium(III) and iron(II) complexes / deg | | | | | |
| O1-Yb1-O2 | 90.1(3)/ 89.9(3) | N4-Fe1-N5 | 88.3(5) | N5-Fe1-N6 | 82.2(4) |
| O1-Yb1-N1 | 91.2(3)/ 88.8(3) | C1-Fe1-N4 | 92.4(5) | N6-Fe1-C2 | 93.2(5) |
| O2-Yb1-N1 | 93.1(3)/ 86.9(3) | C1-Fe1-N3 | 92.3(5) | C2-Fe1-N4 | 174.5(5) |
| O1-Yb1-O1 | 180.0 | N3-Fe1-N4 | 80.8(6) | N5-Fe1-C1 | 175.5(5) |
| O2-Yb1-O2 | 180.0 | N4-Fe1-N6 | 92.0(5) | N3-Fe1-N6 | 171.0(5) |
| N1-Yb1-N1 | 180.0 | N6-Fe1-C1 | 93.3(5) | Yb1-C1≡N1 | 164.3(9) |
| C1-Fe1-C2 | 89.3(6) | C2-Fe1-N3 | 93.8(6) | - | - |
| C2-Fe1-N5 | 90.5(5) | N3-Fe1-N5 | 92.2(4) | - | - |
| details of malononitrile geometry / Å, deg | | | | | |
| N1S≡C1S | 1.223(18) | C3S≡N2S | 1.17(2) | C2S-C2S≡N2S | 170(4) |
| C1S-C2S | 1.389(18) | N1S≡C1S-C2S | 158(5) | - | - |
| C2S-C3S | 1.420(17) | C1S-C2S-C3S | 105(3) | - | - |

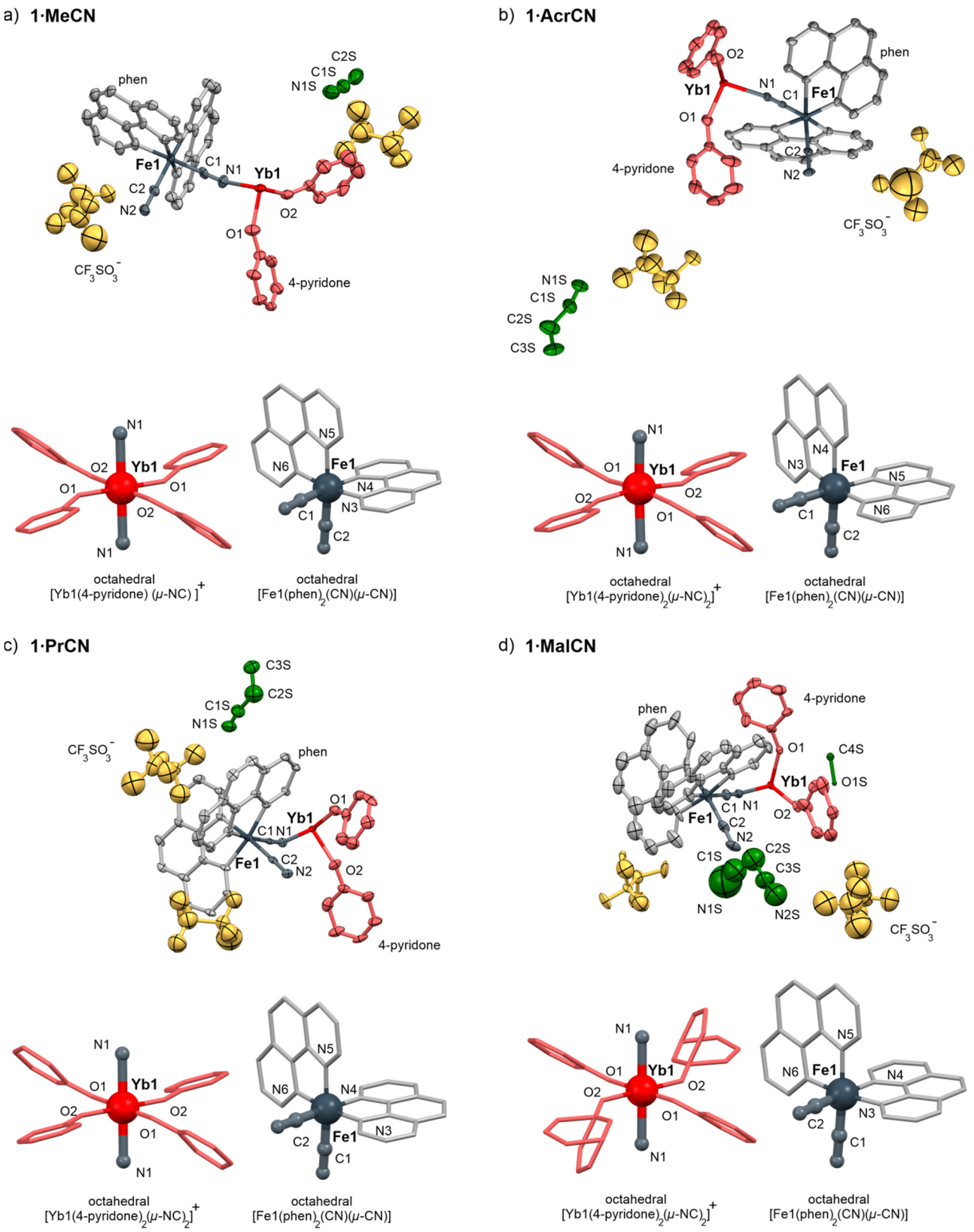


**Figure S3.** Comparison of the crystal structures of **1·MeCN** (a), **1·PrCN** (b), **1·AcrCN** (c), and **1·MalCN** (d) represented by the asymmetric units presented with the selected atoms labelling schemes, and the detailed insights into octahedral Yb1 and Fe1 complexes. Thermal ellipsoids are presented at the 30% probability level. Hydrogen atoms were omitted for clarity.

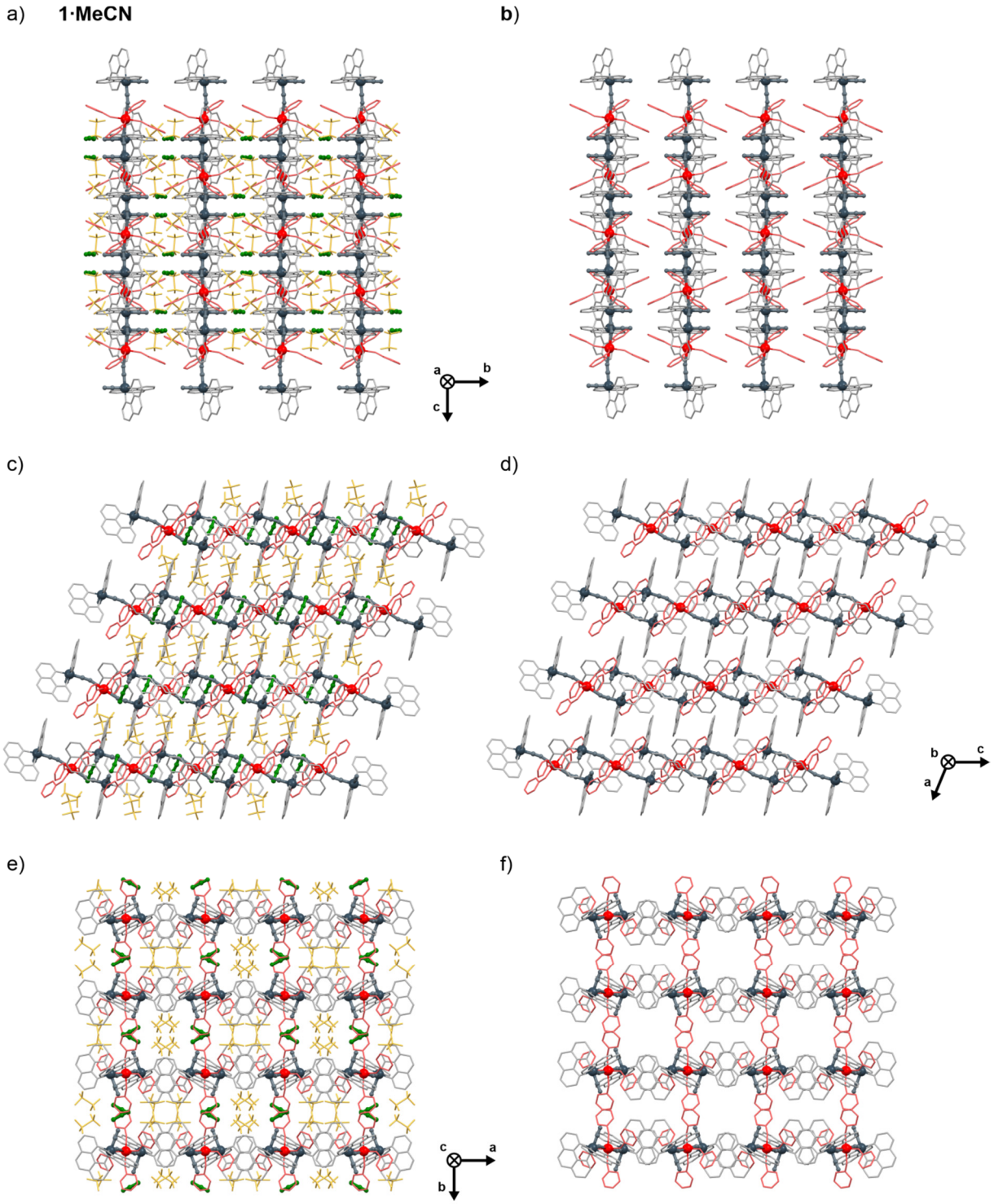


**Figure S4.** The views of the crystal structure of **1·MeCN** along crystallographic *a* (a, b), *b* (c, d), and *c* (e, f) axes. Solvent molecules and anions were presented on the left panel (a, c, and e) while they were omitted for clarity on the right panel (b, d, and f).

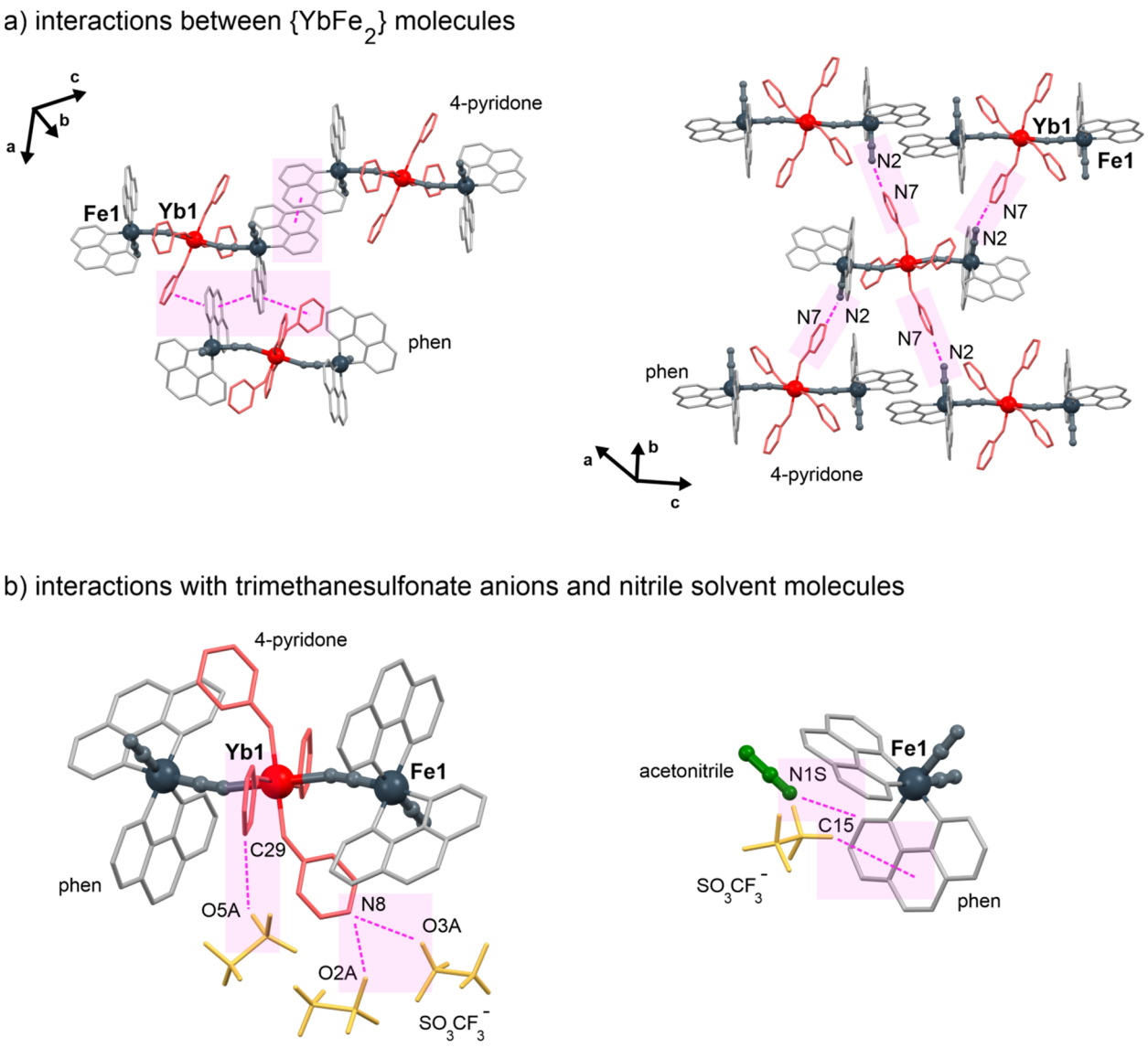


**Figure S5.** The views of supramolecular interactions in the crystal structure of **1·MeCN**, including the interactions between {YbFe2} molecules (a) and between {YbFe2} units and nitrile molecules of crystallization as well as trifluoromethanesulfonate anions (b).

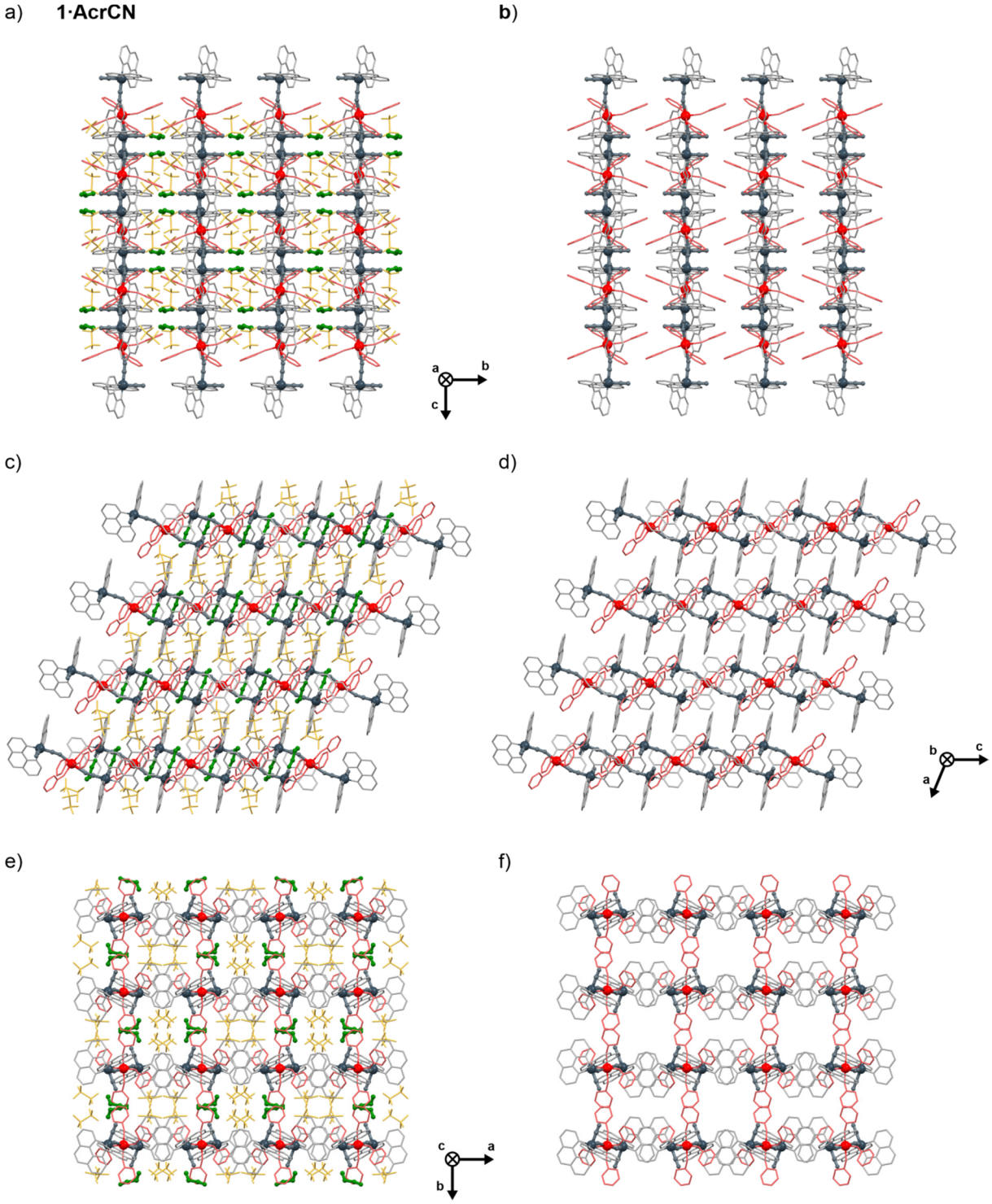


**Figure S6.** The views of the crystal structure of **1·AcrCN** along crystallographic *a* (a, b), *b* (c, d), and *c* (e, f) axes. Solvent molecules and anions were presented on the left panel (a, c, and e) while they were omitted for clarity on the right panel (b, d, and f).

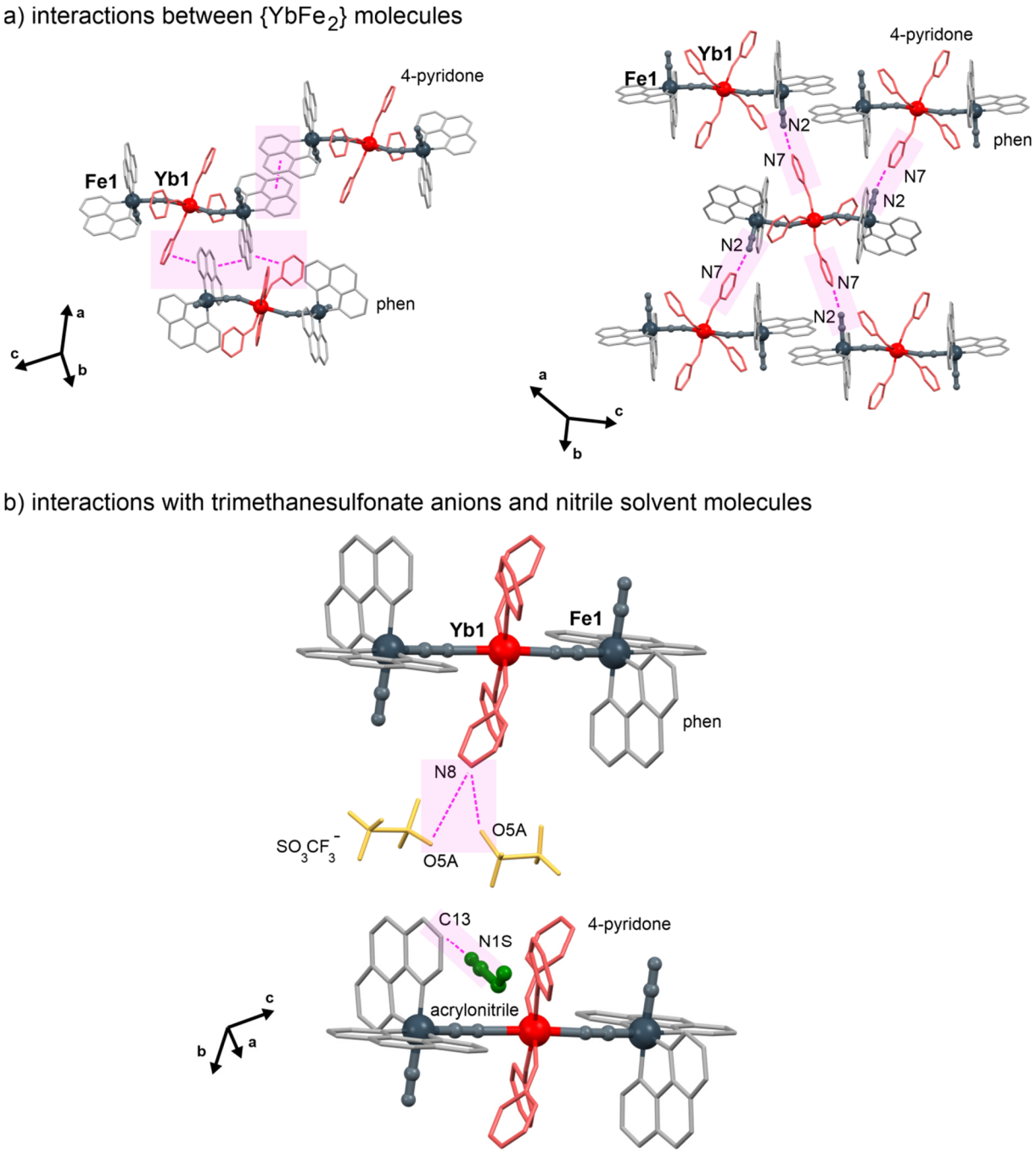


**Figure S7.** The views of supramolecular interactions in the crystal structure of **1·AcrCN**, including the interactions between {YbFe2} molecules (a) and between {YbFe2} units and nitrile molecules of crystallization as well as trifluoromethanesulfonate anions (b).

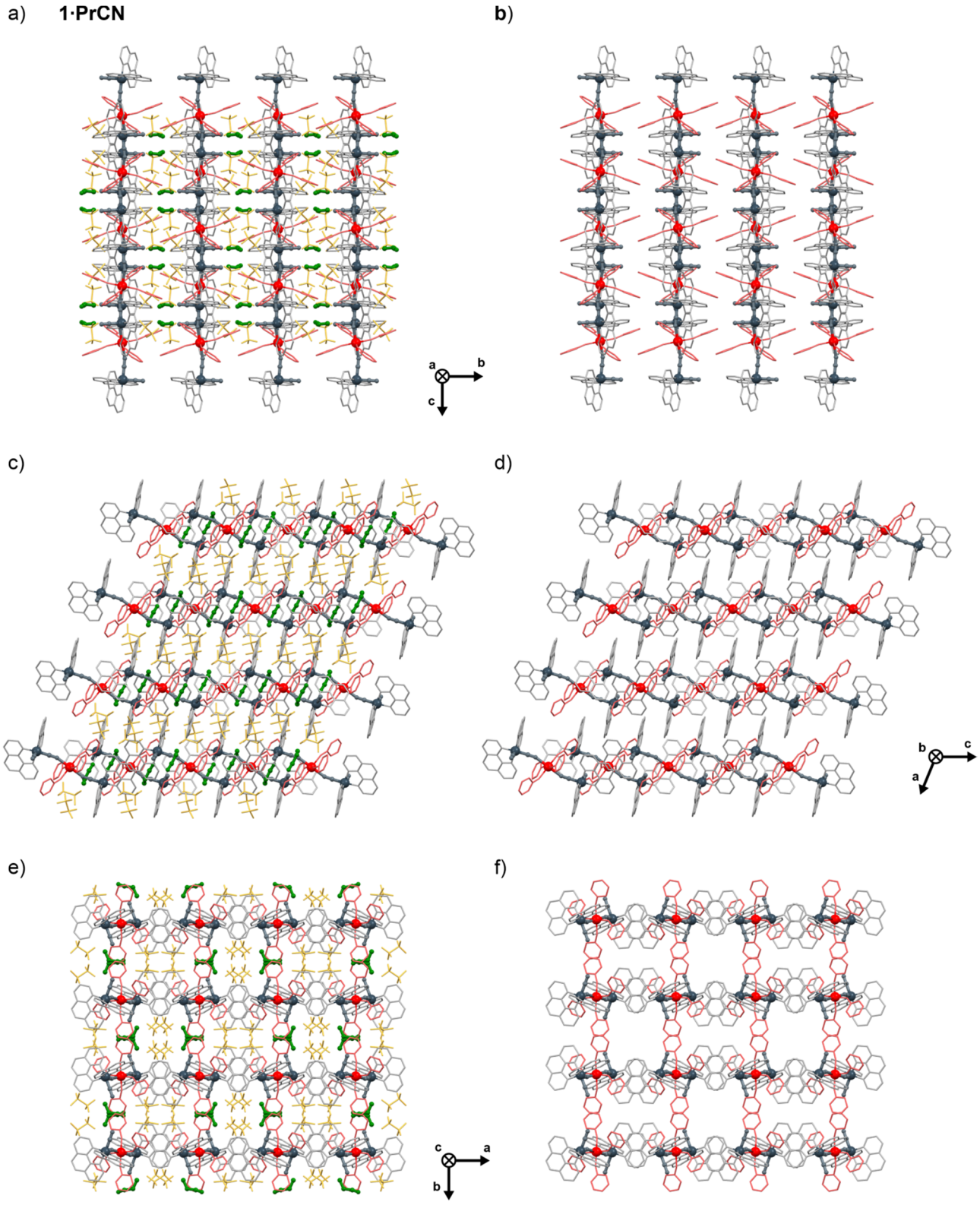


**Figure S8.** The views of the crystal structure of **1·PrCN** along crystallographic *a* (a, b), *b* (c, d), and *c* (e, f) axes. Solvent molecules and anions were presented on the left panel (a, c, and e) while they were omitted for clarity on the right panel (b, d, and f).

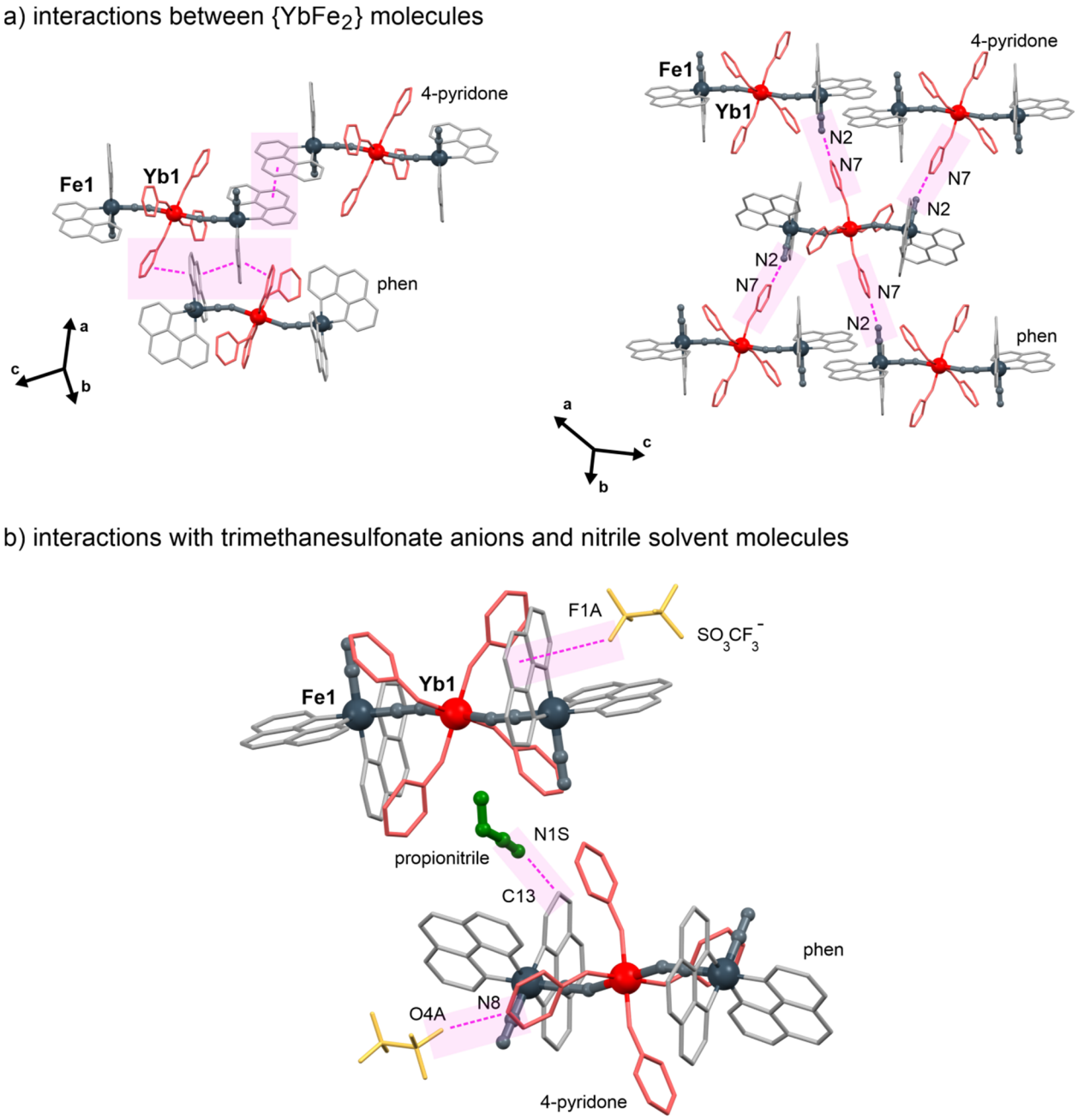


**Figure S9.** The views of the supramolecular interaction between {YbFe2} molecules (a) and between {YbFe2} units and with crystallization nitrile molecules as well as trifluoromethanesulfonate anions (b) in the crystal structure of **1·PrCN**.

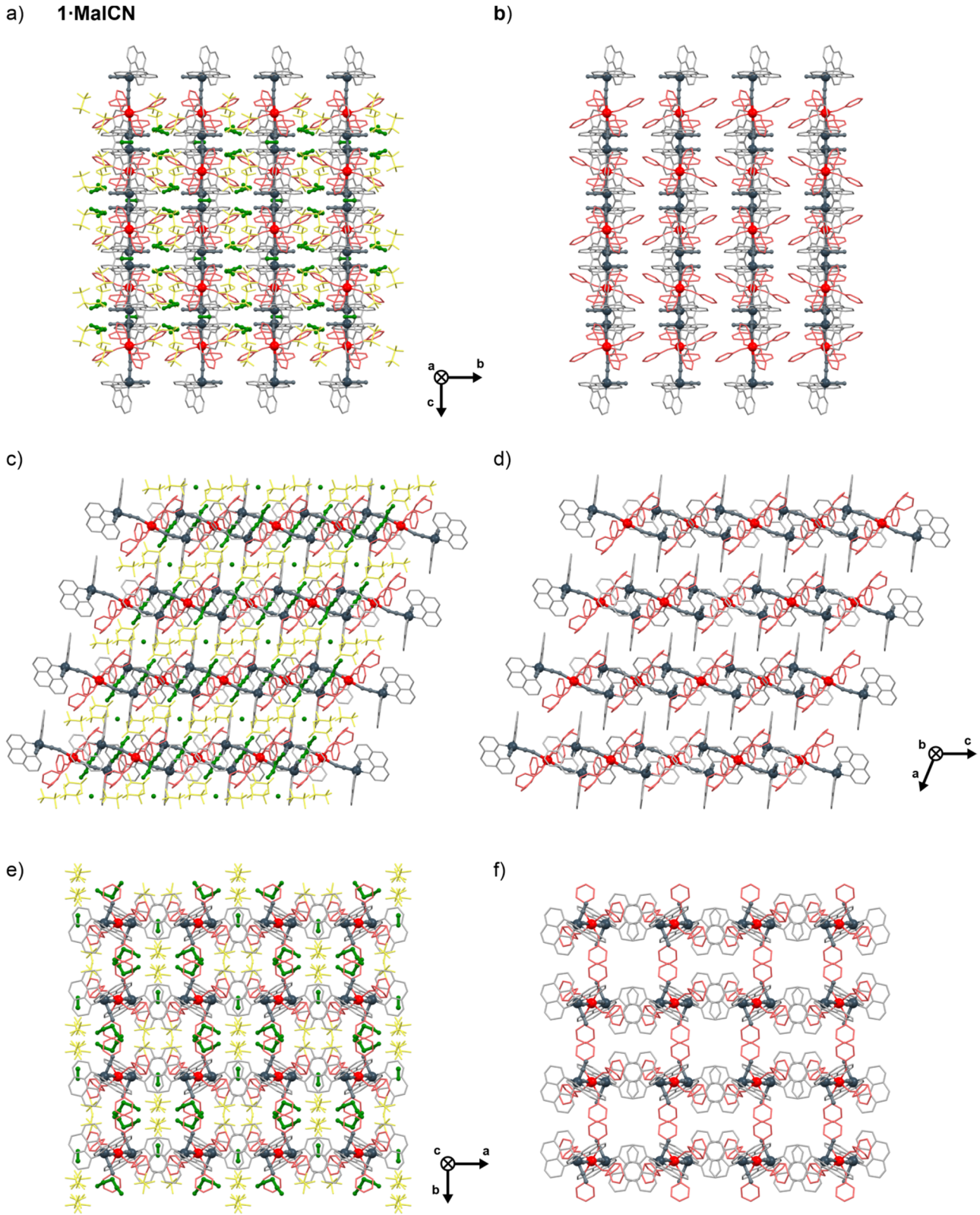


**Figure S10.** The views of the crystal structure of **1·MalCN** along crystallographic *a* (a, b), *b* (c, d), and *c* (e, f) axes. Solvent molecules and anions were presented on the left panel (a, c, and e) while they were omitted for clarity on the right panel (b, d, and f).

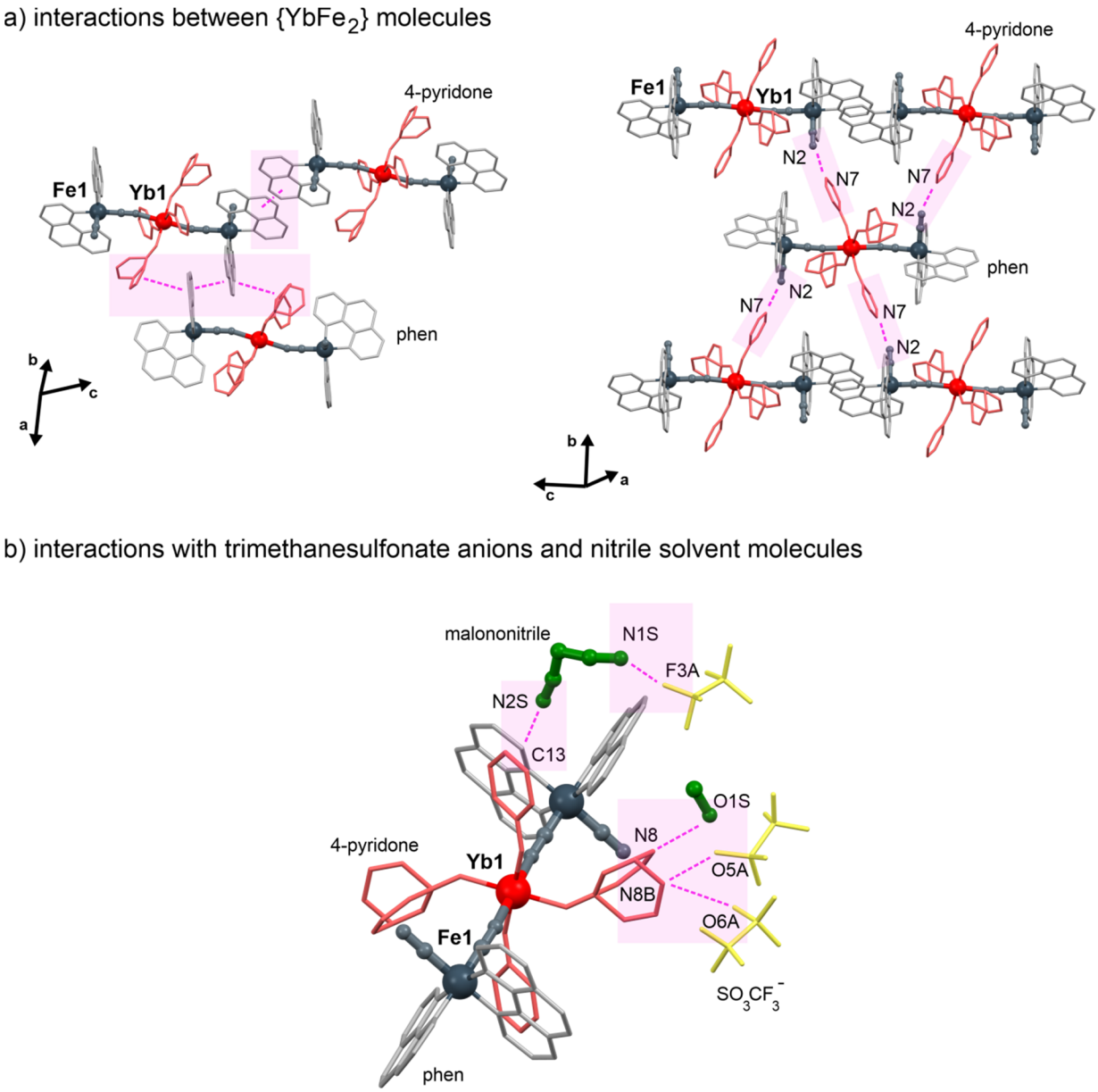


**Figure S11.** The views of the supramolecular interaction between {YbFe2} molecules (a) and between {YbFe2} units and with crystallization nitrile molecules as well as trifluoromethanesulfonate anions (b) in the crystal structure of **1·MalCN**.

**Table S7.** Results of Continuous Shape Measure (CSM) analysis for metal complexes in **1·MeCN**, **1·AcrCN**, **1·PrCN**, and **1·MalCN** (see Figure S3).

| compound | metal complex | CSM parameters* | | | | | determined coordination geometry |
|---|---|---|---|---|---|---|---|
| | | HP-6 | PPY-6 | OC-6 | TPR-6 | JPPY-6 | |
| **1·MeCN** | **[Fe1(phen)$_2$($\mu$-CN)$_2$]** | 31.332 | 27.035 | **0.395** | 14.066 | 30.582 | OC-6 |
| | [Yb1(4-pyridone)$_4$($\mu$-NC)$_2$] | 31.924 | 29.289 | **0.195** | 16.336 | 32.455 | OC-6 |
| **1·AcrCN** | [Fe1(phen)$_2$($\mu$-CN)$_2$] | 30.733 | 27.353 | **0.376** | 14.593 | 30.903 | OC-6 |
| | [Yb1(4-pyridone)$_4$($\mu$-NC)$_2$] | 32.368 | 29.564 | **0.232** | 16.419 | 32.791 | OC-6 |
| **1·PrCN** | [Fe1(phen)$_2$($\mu$-CN)$_2$] | 31.049 | 27.547 | **0.306** | 14.736 | 31.090 | OC-6 |
| | [Yb1(4-pyridone)$_4$($\mu$-NC)$_2$] | 31.756 | 29.269 | **0.163** | 16.279 | 32.468 | OC-6 |
| **1·MalCN** | [Fe1(phen)$_2$($\mu$-CN)$_2$] | 30.726 | 27.704 | **0.343** | 14.852 | 31.260 | OC-6 |
| | [Yb1(4-pyridone)$_4$($\mu$-NC)$_2$] | 31.734 | 29.359 | **0.162** | 16.350 | 32.620 | OC-6 |

*CSM parameters for six-coordinated complexes [S6,S7]:

CSM HP-6 - the parameter related to the hexagon ($D_{6h}$ symmetry)
CSM PPY-6 - the parameter related to the pentagonal pyramid ($C_{5v}$)
CSM OC-6 - the parameter related to the octahedron ($O_h$)
CSM TPR-6 - the parameter related to the trigonal prism ($D_{3h}$)
CSM JPPY-6 - the parameter related to the Johnson pentagonal pyramid ($C_{5v}$)

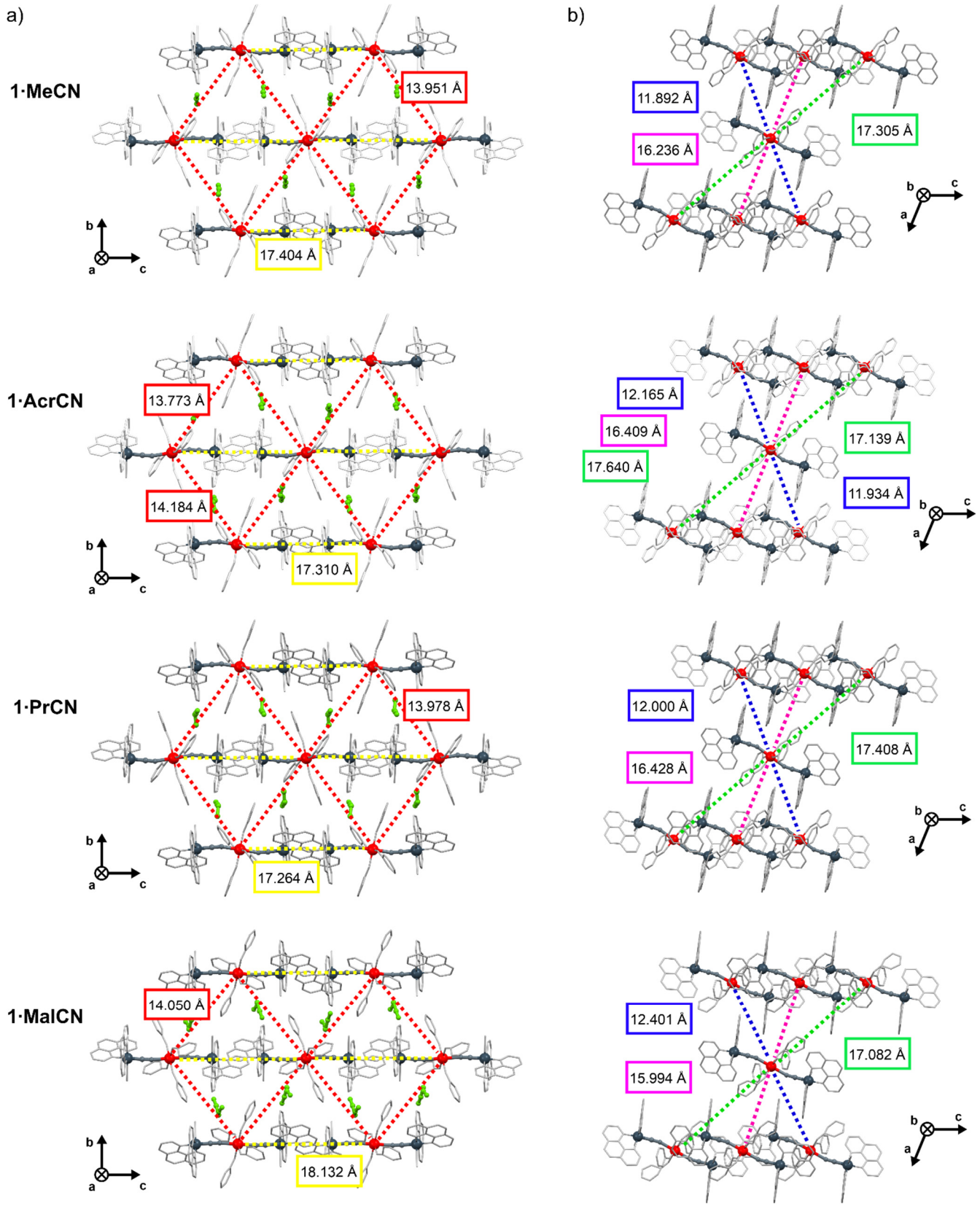


**Figure S12.** The visualization of representative Yb···Yb distances in the crystal structures of **1·MeCN**, **1·AcrCN**, **1·PrCN**, and **1·MalCN** presented within the crystallographic *bc* (a) and *ac* planes (b). See Table S8 for detailed comparison of the related values of Yb···Yb distances.

**Table S8.** Comparison of clostest Yb···Yb distances in the crystal structures of **1·MeCN**, **1·AcrCN**, **1·PrCN**, and **1·MalCN** (see Figure S12 for visualization).

| crystallographic direction | Yb1-Yb1 distance / Å | | | |
|---|---|---|---|---|
| | **1·MeCN** | **1·AcrCN** | **1·PrCN** | **1·MalCN** |
| within the *bc* plane | | | | |
| (011) | 13.951 | 13.979* | 13.978 | 14.050 |
| (001) | 17.404 | 17.310 | 17.264 | 18.132 |
| within the *ac* plane | | | | |
| (101) | 11.892 | 12.050* | 12.000 | 12.401 |
| (110) | 16.236 | 16.409 | 16.428 | 15.994 |
| $(10\bar{1})$ | 17.305 | 17.390* | 17.408 | 17.082 |

*average value

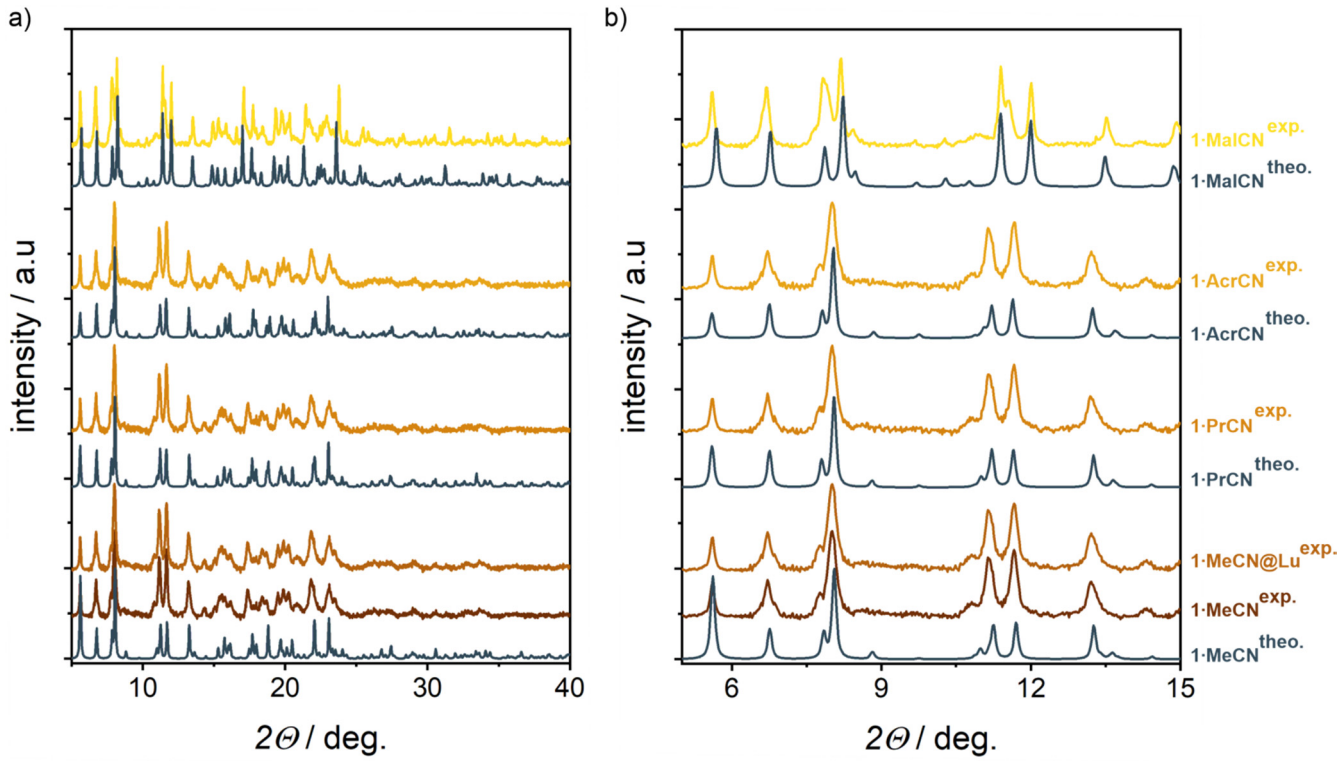


**Figure S13.** Experimental powder X-ray (P-XRD) patterns of **1·MeCN**, **1·AcrCN**, **1·PrCN**, and **1·MalCN** presented in the broad 2Θ range of 5–40° (a) and the enlarged view of the limited 5–15° range (b). The experimental patterns were compared with the PXRD patterns calculated from the respective structural models obtained within the single-crystal X-ray diffraction (SC-XRD) structural analysis.

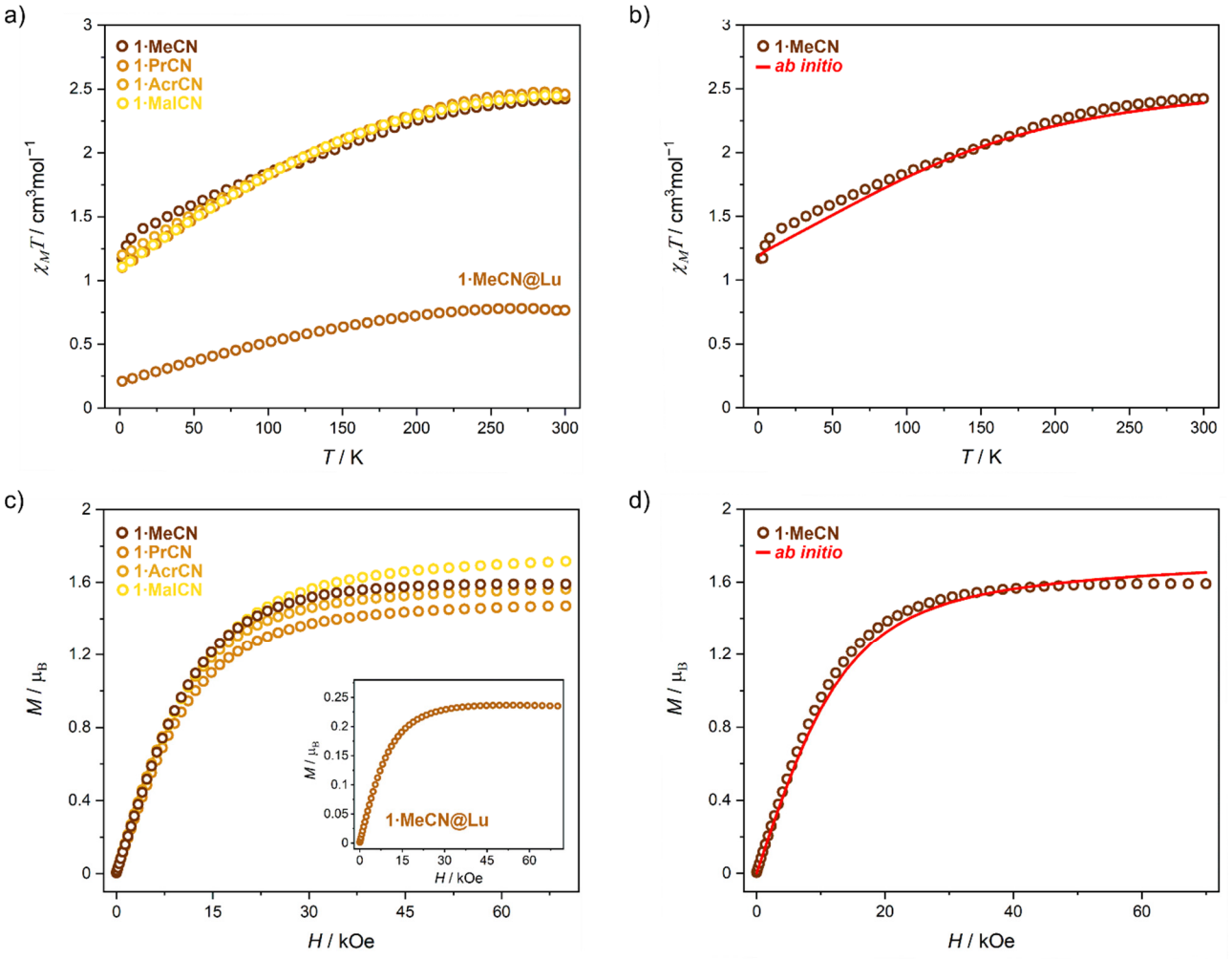


**Figure S14.** Direct-current (*dc*) magnetic characteristics of **1·MeCN**, **1·PrCN**, **1·AcrCN, 1·MalCN** (main graphs), and **1·MeCN@Lu** (the insets): temperature dependences of the $\chi_M T$ product under the external magnetic field of $H_{dc}$ = 1000 Oe (a), and field dependences of molar magnetization ($M$) collected at $T$ = 1.8 K (c), together with the comparison of the experimental $\chi_M T(T)$ and $M(H)$ curves for **1·MeCN** and the theoretical ones, obtained using the *ab initio* calculations (model **1L**, Tables S9 and S11) (b and d for $\chi_M T(T)$ and $M(H)$ plots, respectively).

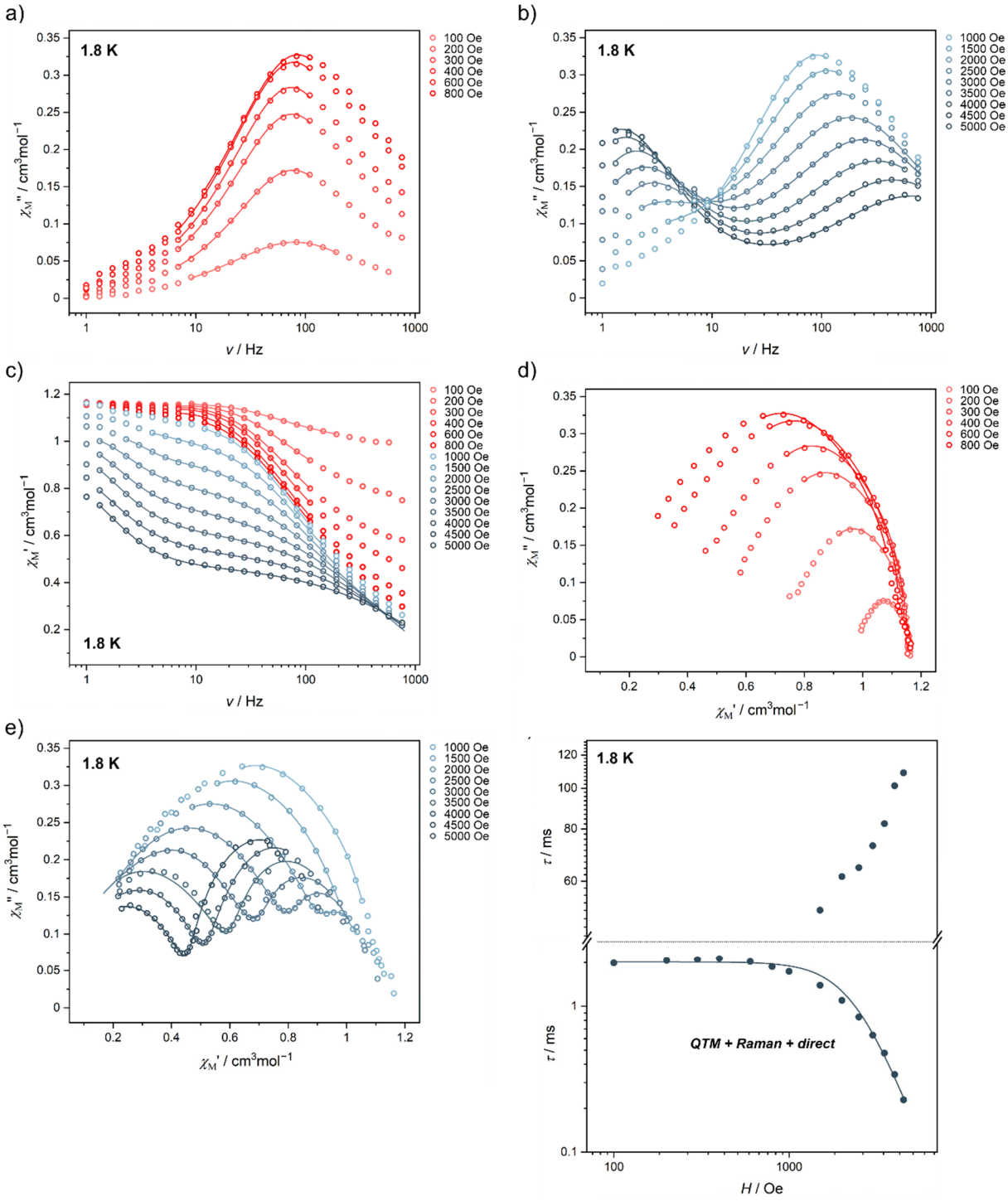


**Figure S15.** Magnetic–field–variable alternate–current (*ac*) magnetic characteristics of **1·MeCN** at $T$ = 1.8 K, and their analysis: the frequency dependences of the out-of-phase susceptibility, $\chi_M''$, under variable indicated *dc* fields (a, b), the frequency dependences of the in-phase susceptibility, $\chi_M'$, under indicated *dc* fields (c), the related Argand plots (d, e), and the field-dependence of relaxation time, $\tau$ for two analyzed relaxation processes (f). Colored solid curves in (a–e) represent the best-fits using the generalized Debye model for a single or a double relaxation processes (depending on the shape of *ac* curves, see comment to Figures S15–S24). Solid line in (f) show the best-fit taking into account QTM, a Raman process, and a direct process (Equation 1). Best-fit parameters are gathered in Table 1.

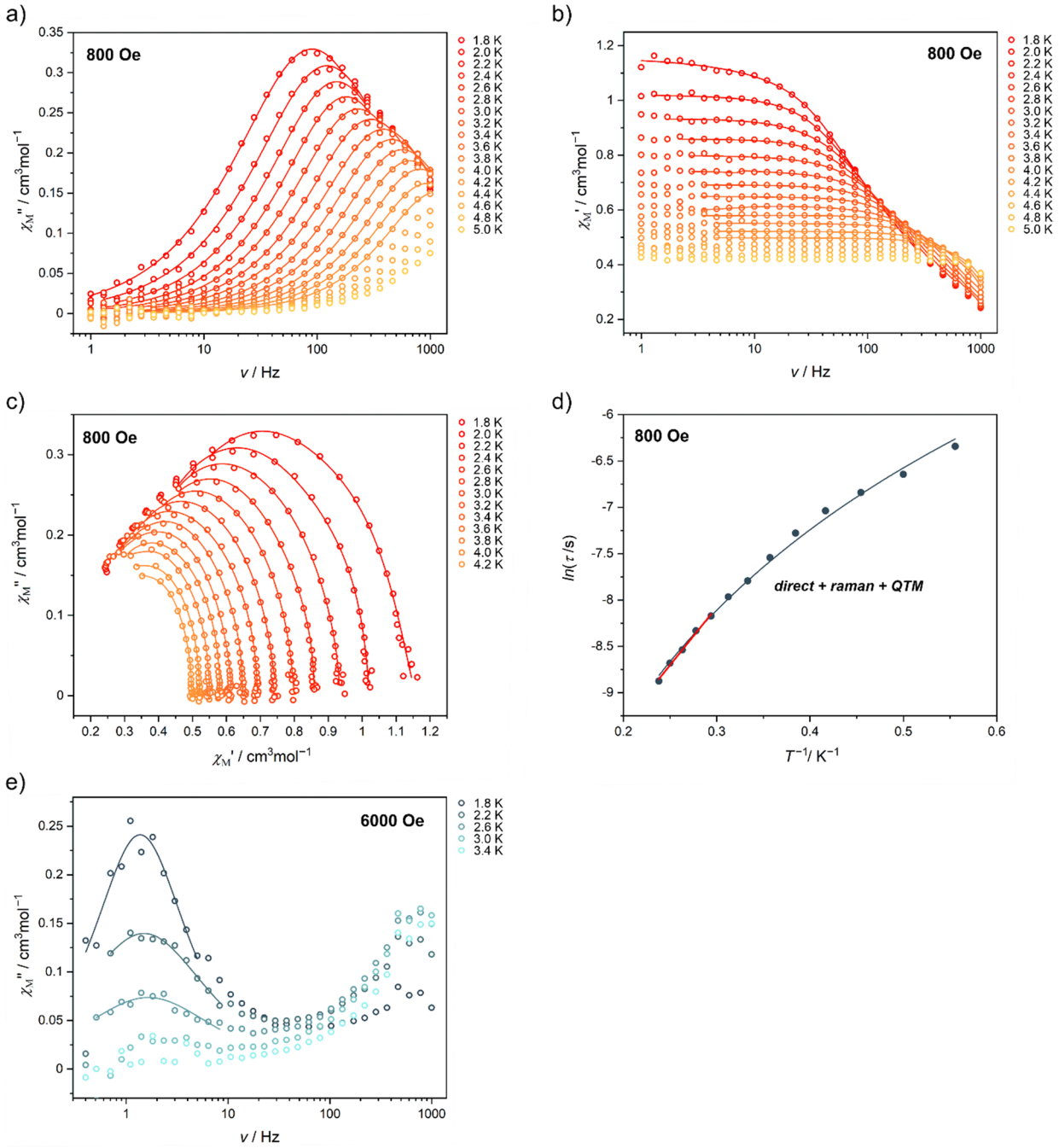


**Figure S16.** Temperature–variable alternate–current (*ac*) magnetic characteristics of **1·MeCN** under $H_{dc}$ of 800 Oe (a-d) or 6000 Oe (e), and their analysis: the frequency dependences of the out-of-phase susceptibility, $\chi_M''$, at various indicated temperatures under $H_{dc}$ = 800 Oe (a), the frequency dependences of the in-phase susceptibility, $\chi_M'$, at various indicated temperatures under $H_{dc}$ = 800 Oe (b), the related Argand plots (c), the temperature dependence of the resulting relaxation time, $\tau$ (d), and the frequency dependences of the $\chi_M''$ at various indicated temperatures under $H_{dc}$ = 6000 Oe (e). Colored solid curves in (a-c, e) represent the best-fits using the generalized Debye model for a single relaxation process. Solid blue line in (d) show the best-fit taking into account QTM, a Raman process, and a field-induced direct process (equation 1), while red line represents the linear fitting following the Arrhenius law for the limited temperature range of 3.4–4.2 K. Best-fit parameters are gathered in Table 1.

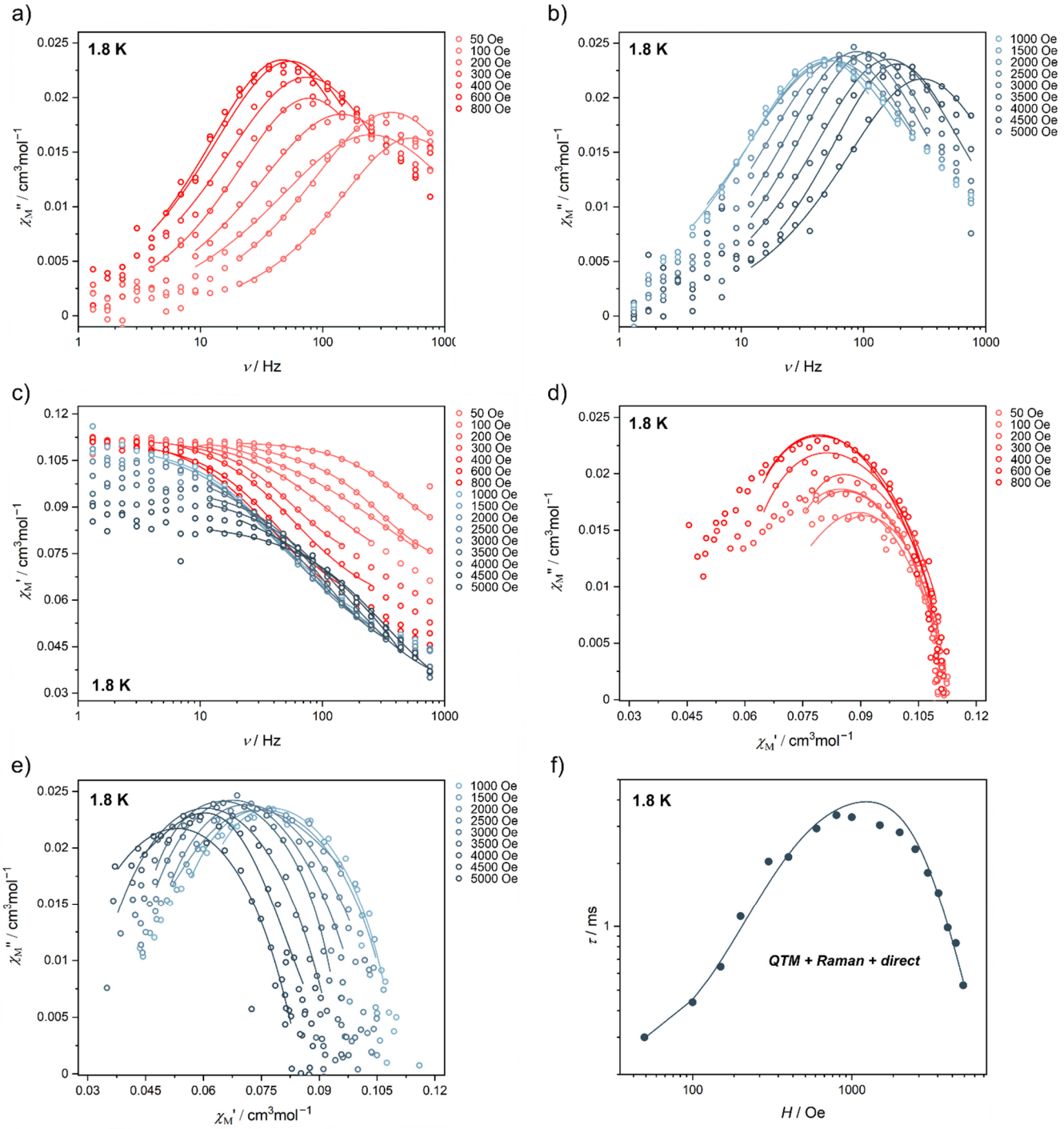


**Figure S17.** Magnetic–field–variable alternate–current (*ac*) magnetic characteristics of **1·MeCN@Lu** at $T = 1.8$ K, and their analysis: the frequency dependences of the out-of-phase susceptibility, $\chi_M''$, under variable indicated *dc* fields (a, b), the frequency dependences of the in-phase susceptibility, $\chi_M'$, under indicated *dc* fields (c), the related Argand plots (d, e), and the field-dependence of resulting relaxation time, $\tau$ (f). Colored solid curves in (a–e) represent the best-fits using the generalized Debye model for a single relaxation process (see comment to Figures S15–S24). Solid line in (f) show the best-fit taking into account QTM, a Raman process, and a direct process (Equation 1). Best-fit parameters are gathered in Table 1.

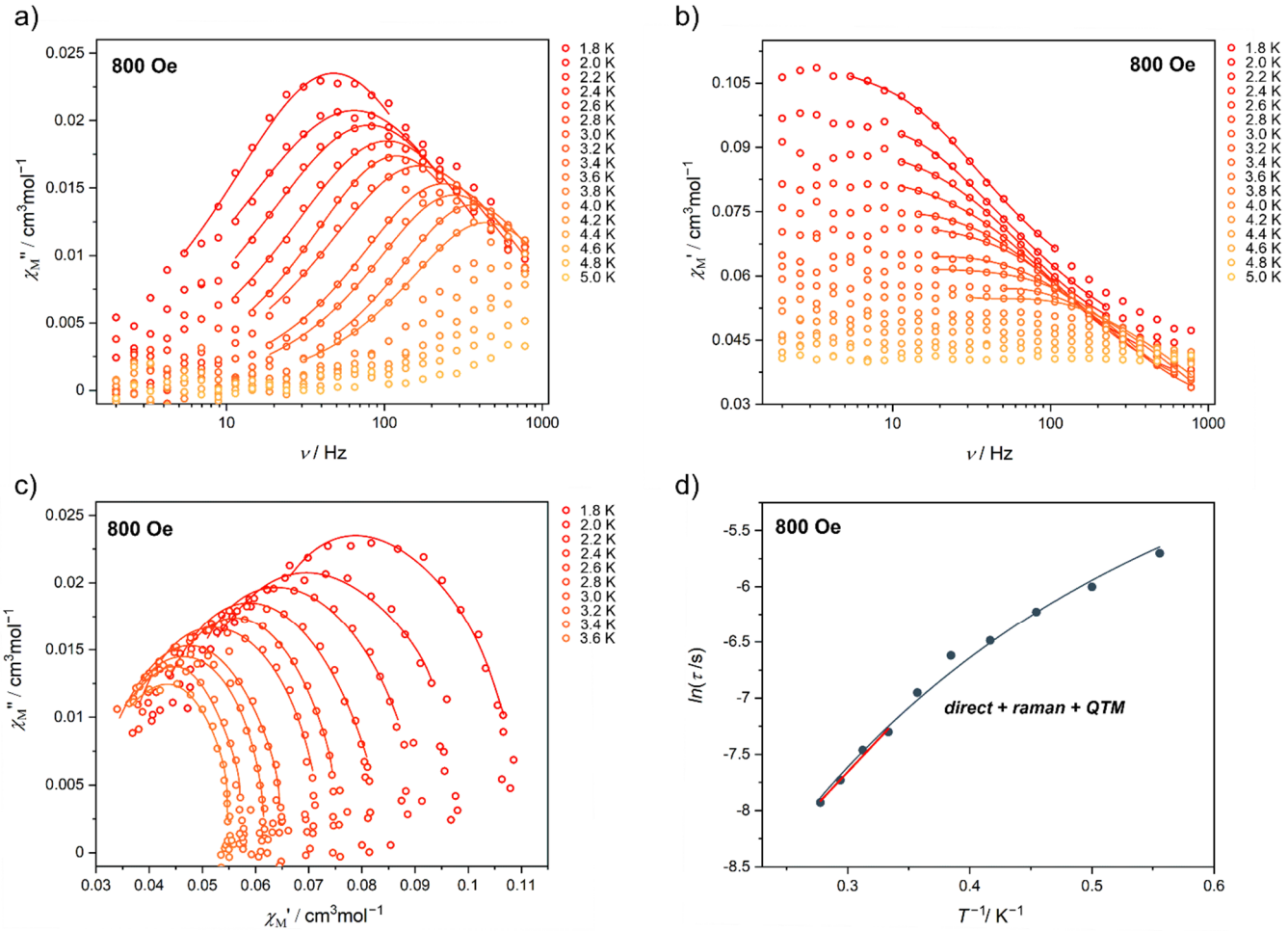


**Figure S18.** Temperature–variable alternate–current (*ac*) magnetic characteristics of **1·MeCN@Lu** under $H_{dc}$ = 800 Oe and their analysis: the frequency dependences of the out-of-phase susceptibility, $\chi_M''$, at various indicated temperatures (a), the frequency dependences of the in-phase susceptibility, $\chi_M'$, at indicated temperatures (b), the related Argand plots (c), and the temperature dependence of the resulting relaxation time, $\tau$ (d). Colored solid curves in (a-c) represent the best-fits using the generalized Debye model for a single relaxation process. Solid blue line in (d) show the best-fit taking into account QTM, a Raman process, and a field-induced direct process (equation 1), while red line represents the linear fitting following the Arrhenius law for the limited temperature range of 3.0–3.6 K. Best-fit parameters are gathered in Table 1.

**Table S9.** Description of the basis sets (two models: **1S** and **1L**) employed in the *ab initio* calculations of the $Yb^{III}$ crystal field in **1·MeCN**.

| **Basis set 1S** | **Basis set 1L** |
|---|---|
| Yb.ANO-RCC-VDZP 7S6P4D2F1G | Yb.ANO-RCC-VTZP 8S7P5D3F2G1H |
| Fe.ANO-RCC-VDZ 5S4P2D | Fe.ANO-RCC-VDZ 5S4P2D |
| O.ANO-RCC-VDZ 3S2P | O.ANO-RCC-VDZP 3S2P1D |
| C.ANO-RCC-VDZ 3S2P | C.ANO-RCC-VDZ 3S2P |
| H.ANO-RCC-VDZ 2S | H.ANO-RCC-VDZ 2S |
| N.ANO-RCC-VDZ 3S2P | N.ANO-RCC-VDZP 3S2P1D (first coordination sphere) |
| | N.ANO-RCC-VDZ 3S2P (others) |

**Table S10.** Summary of the energy splitting of the $^2F_{7/2}$ multiplet of Yb(III) in **1S** model, together with pseudo-$g$-tensors of each Kramers doublet.

| **Energy / cm$^{-1}$** | **Pseudo-$g$-tensor components** | | |
|---|---|---|---|
| | $g_x$ | $g_y$ | $g_z$ |
| 0.000 | 0.8137 | 1.6506 | 5.3426 |
| 237.714 | 0.4719 | 0.9739 | 4.0118 |
| 302.622 | 0.3155 | 0.5902 | 2.6562 |
| 509.498 | 1.9539 | 2.6213 | 5.1813 |
| **State composition**, $\|m_J\rangle$ (only components with contribution above 1%) of the ground Kramers doublet | | | |
| 64.8% $\|-7/2\rangle$<br>21.7% $\|+1/2\rangle$<br>6.4% $\|-1/2\rangle$<br>4.6% $\|-5/2\rangle$<br>1.5% $\|+7/2\rangle$ | | 64.8% $\|+7/2\rangle$<br>21.7% $\|-1/2\rangle$<br>6.4% $\|+1/2\rangle$<br>4.6% $\|+5/2\rangle$<br>1.5% $\|-7/2\rangle$ | |

**Table S11.** Summary of the energy splitting of the $^2F_{7/2}$ multiplet of Yb(III) in **1L** model, together with pseudo-*g*-tensors of each Kramers doublet.

| **Energy / cm$^{-1}$** | **Pseudo-*g*-tensor components** | | |
|---|---|---|---|
| | $g_x$ | $g_y$ | $g_z$ |
| 0.000 | 0.5627 | 1.3436 | 5.9528 |
| 280.425 | 0.3163 | 0.7647 | 4.4613 |
| 342.877 | 0.3428 | 1.6212 | 3.2072 |
| 551.166 | 1.7344 | 3.0360 | 4.8500 |
| **State composition**, $\left\|m_J\right\rangle$ (only components with contribution above 1%) of the ground Kramers doublet | | | |
| 76.9% $\left\|-7/2\right\rangle$<br>19.4% $\left\|+1/2\right\rangle$<br>2.3% $\left\|-1/2\right\rangle$ | | 76.9% $\left\|+7/2\right\rangle$<br>19.4% $\left\|-1/2\right\rangle$<br>2.3% $\left\|+1/2\right\rangle$ | |

**Table S12.** The energy splitting of the excited $^2F_{5/2}$ multiplet of Yb(III) complexes extracted from the *ab initio* calculations using **1S** and **1L** models.

| **Basis set 1S** | **Basis set 1L** |
|---|---|
| 10522.427 cm$^{-1}$ | 10371.499 cm$^{-1}$ |
| 10657.785 cm$^{-1}$ | 10560.202 cm$^{-1}$ |
| 10905.252 cm$^{-1}$ | 10793.624 cm$^{-1}$ |

**Comment to the *ab initio* calculations**

*Ab initio* calculations were performed using the crystal structure of **1·MeCN** taken from the single-crystal X-Ray diffraction experiment. Calculated molecular fragment consisted of the whole cationic $\{YbFe_2\}^{3+}$ unit but without solvent molecules of crystallization and counter-ions (see Figure 1). To examine local magnetic properties of Yb(III) centers, State Average Complete Active Space Self-Consistent Field (SA-CASSCF) calculations were performed using OpenMolcas software [S8]. Scalar relativistic effects were taken into account by employing two-component second-order Douglas-Kroll-Hess (DKH2) Hamiltonian together with relativistic Atomic Natural Orbital basis sets - ANO-RCC type [S9–S11]. To save disk space for computations of this relatively big cluster (over 150 atoms and around 1200 basis functions), the Cholesky decomposition of ERI-s (electron repulsion integrals) was used with the $1.0 \cdot 10^{-8}$ threshold. Two models were considered: the first one – smaller (**S**) - with VDZP basis function quality for Yb(III) centers and VDZ for other atoms, and – larger (**L**) – using VTZP for Yb(III) centers, VDZP for atoms directly bonded to the magnetic center in the first coordination sphere, and VDZ for the others. Descriptions of employed basis sets and their contractions are presented in Table S9. In the CASSCF step, the active space was composed of seven 4f-orbitals of Yb(III) with 13 active electrons – CAS(13in7), and 7 doublets spin-adapted states arising from different possible electrons distributions in 4f orbitals were evaluated. In the next step, all previously optimized, as spin-free, states were mixed within the Restricted Active Space State Interaction (RASSI) submodule by Spin-Orbit-Coupling (SOC) within the atomic mean-field (AMFI) approximation [S12, S13]. In the final step, resulting 14 spin-orbit states were analyzed using the SINGLE_ANISO module to obtain main magnetic axes and pseudo-$g$-tensors of each Krammers doublet, simulate $\chi_M(T)$ and $M(H)$ magnetic dependences, and to decompose the ground SO states into ones with a definite projection of the total momentum on the located quantization z-axis [S14, S15]. The energy splitting of the ground $^2F_{7/2}$ multiplet together with pseudo-$g$-tensor components and the composition of the ground doublet in the $|J = 9/2, m_J>$ basis are presented in Tables S10–S11. In addition, the calculated energy splitting of the excited $^2F_{5/2}$ multiplet of Yb(III) complexes using both models was shown in Table S12.

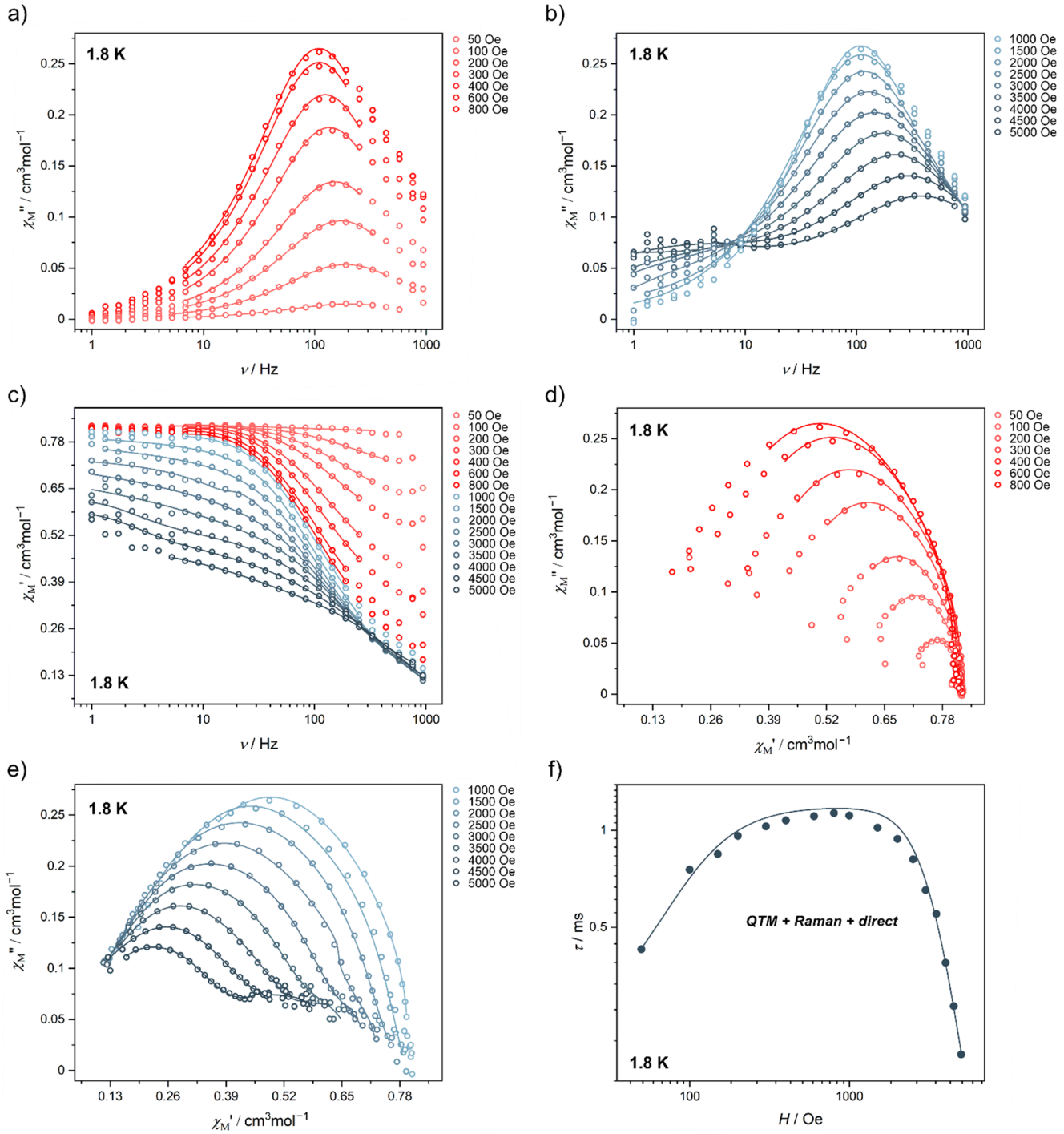


**Figure S19.** Magnetic–field–variable alternate–current (*ac*) magnetic characteristics of **1·AcrCN** at $T$ = 1.8 K, and their analysis: the frequency dependences of the out-of-phase susceptibility, $\chi_M''$, under variable indicated *dc* fields (a, b), the frequency dependences of the in-phase susceptibility, $\chi_M'$, under indicated *dc* fields (c), the related Argand plots (d, e), and the field-dependence of resulting relaxation time, $\tau$ (f). Colored solid curves in (a–e) represent the best-fits using the generalized Debye model for a single or a double relaxation processes (depending on the shape of the *ac* curve; slower relaxation process was not further analyzed; see comment to Figures S15–S24). Solid line in (f) show the best-fit taking into account QTM, a Raman process, and a direct process (Equation 1). Best-fit parameters are gathered in Table 1.

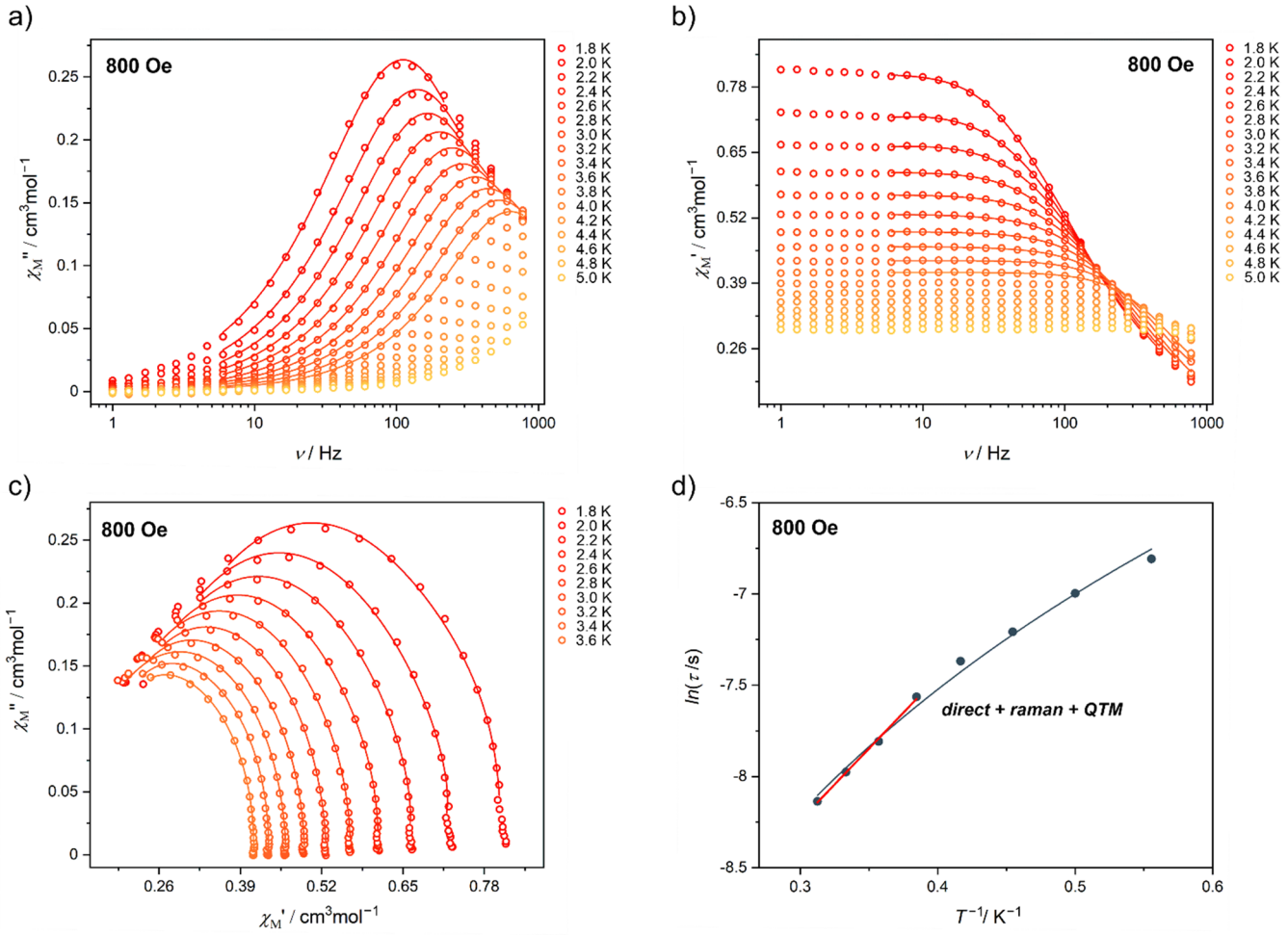


**Figure S20.** Temperature–variable alternate–current (*ac*) magnetic characteristics of **1·AcrCN** under $H_{dc}$ = 800 Oe and their analysis: the frequency dependences of the out-of-phase susceptibility, $\chi_M''$, at various indicated temperatures (a), the frequency dependences of the in-phase susceptibility, $\chi_M'$, at indicated temperatures (b), the related Argand plots (c), and the temperature dependence of the resulting relaxation time, $\tau$ (d). Colored solid curves in (a-c) represent the best-fits using the generalized Debye model for a single relaxation process. Solid blue line in (d) show the best-fit taking into account QTM, a Raman process, and a field-induced direct process (equation 1), while red line represents the linear fitting following the Arrhenius law for the limited temperature range of 2.6–3.2 K. Best-fit parameters are gathered in Table 1.

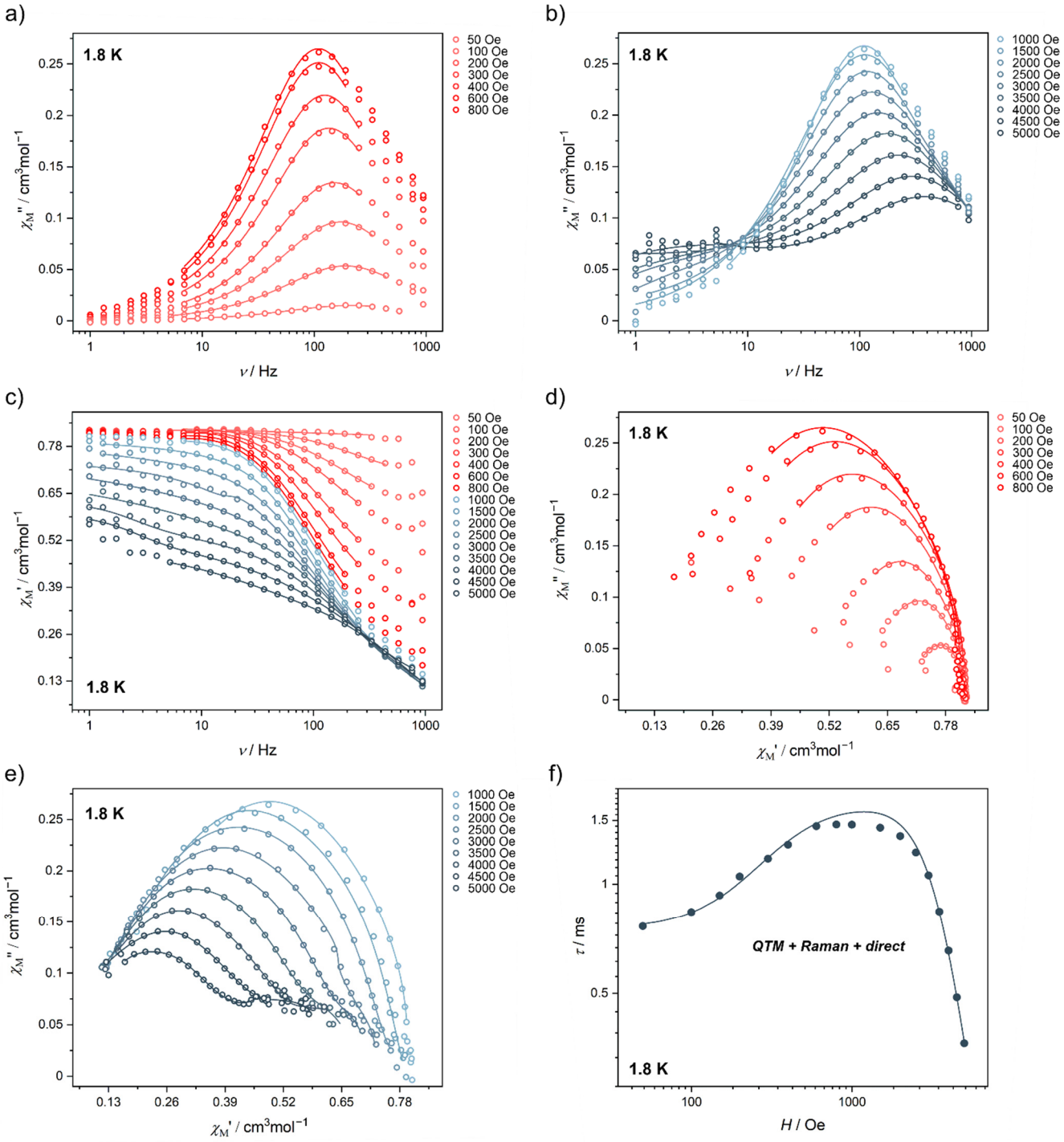


**Figure S21.** Magnetic–field–variable alternate–current (*ac*) magnetic characteristics of **1·PrCN** at $T$ = 1.8 K, and their analysis: the frequency dependences of the out-of-phase susceptibility, $\chi_M''$, under variable indicated *dc* fields (a, b), the frequency dependences of the in-phase susceptibility, $\chi_M'$, under indicated *dc* fields (c), the related Argand plots (d, e), and the field-dependence of resulting relaxation time, $\tau$ (f). Colored solid curves in (a–e) represent the best-fits using the generalized Debye model for a single or a double relaxation processes (depending on the shape of the *ac* curve; slower relaxation process was not further analyzed; see comment to Figures S15–S24). Solid line in (f) show the best-fit taking into account QTM, a Raman process, and a direct process (Equation 1). Best-fit parameters are gathered in Table 1.

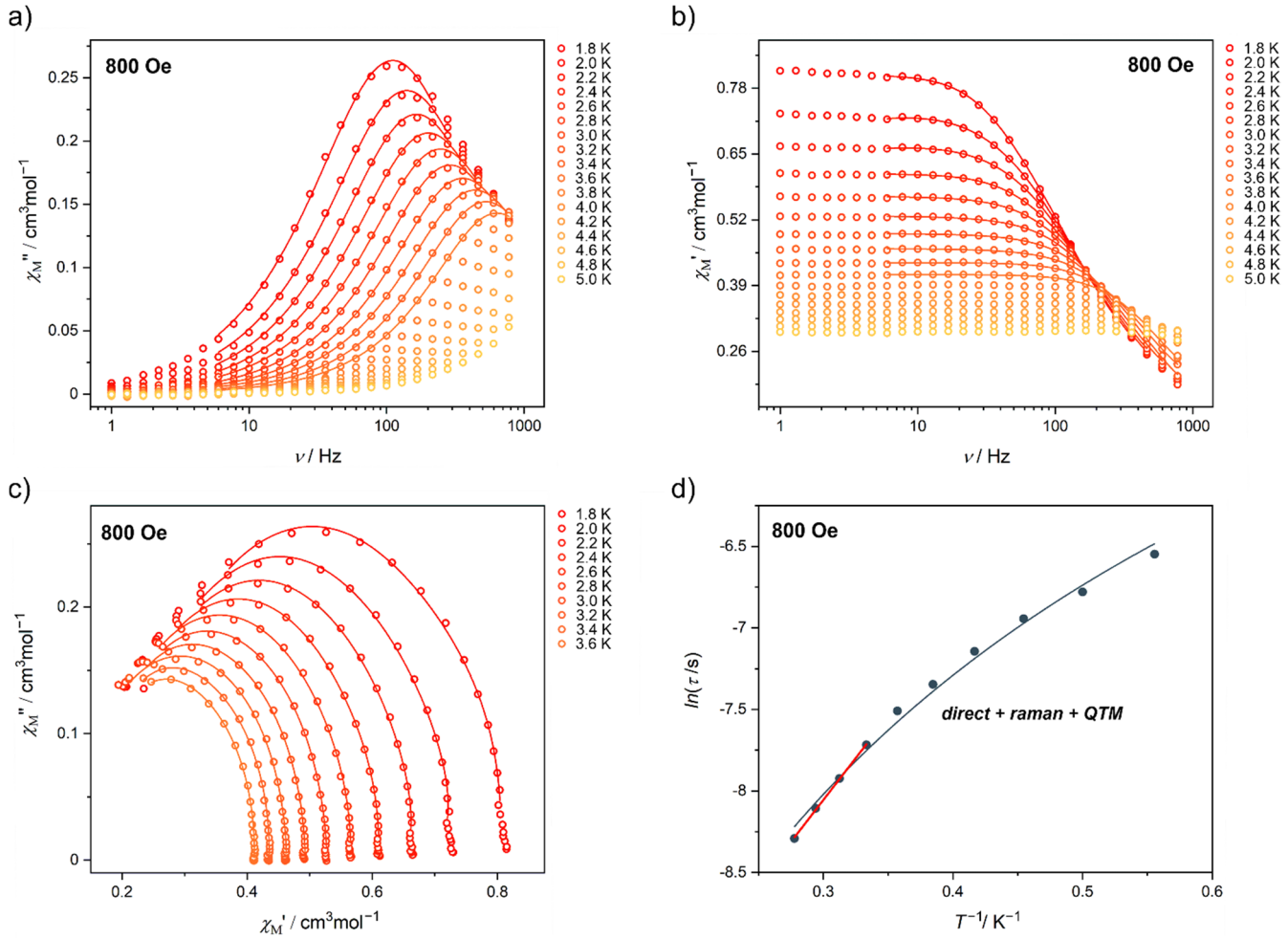


**Figure S22.** Temperature–variable alternate–current (*ac*) magnetic characteristics of **1·PrCN** under $H_{dc}$ = 800 Oe and their analysis: the frequency dependences of the out-of-phase susceptibility, $\chi_M''$, at various indicated temperatures (a), the frequency dependences of the in-phase susceptibility, $\chi_M'$, at indicated temperatures (b), the related Argand plots (c), and the temperature dependence of the resulting relaxation time, $\tau$ (d). Colored solid curves in (a-c) represent the best-fits using the generalized Debye model for a single relaxation process. Solid blue line in (d) show the best-fit taking into account QTM, a Raman process, and a field-induced direct process (equation 1), while red line represents the linear fitting following the Arrhenius law for the limited temperature range of 3.0–3.6 K. Best-fit parameters are gathered in Table 1.

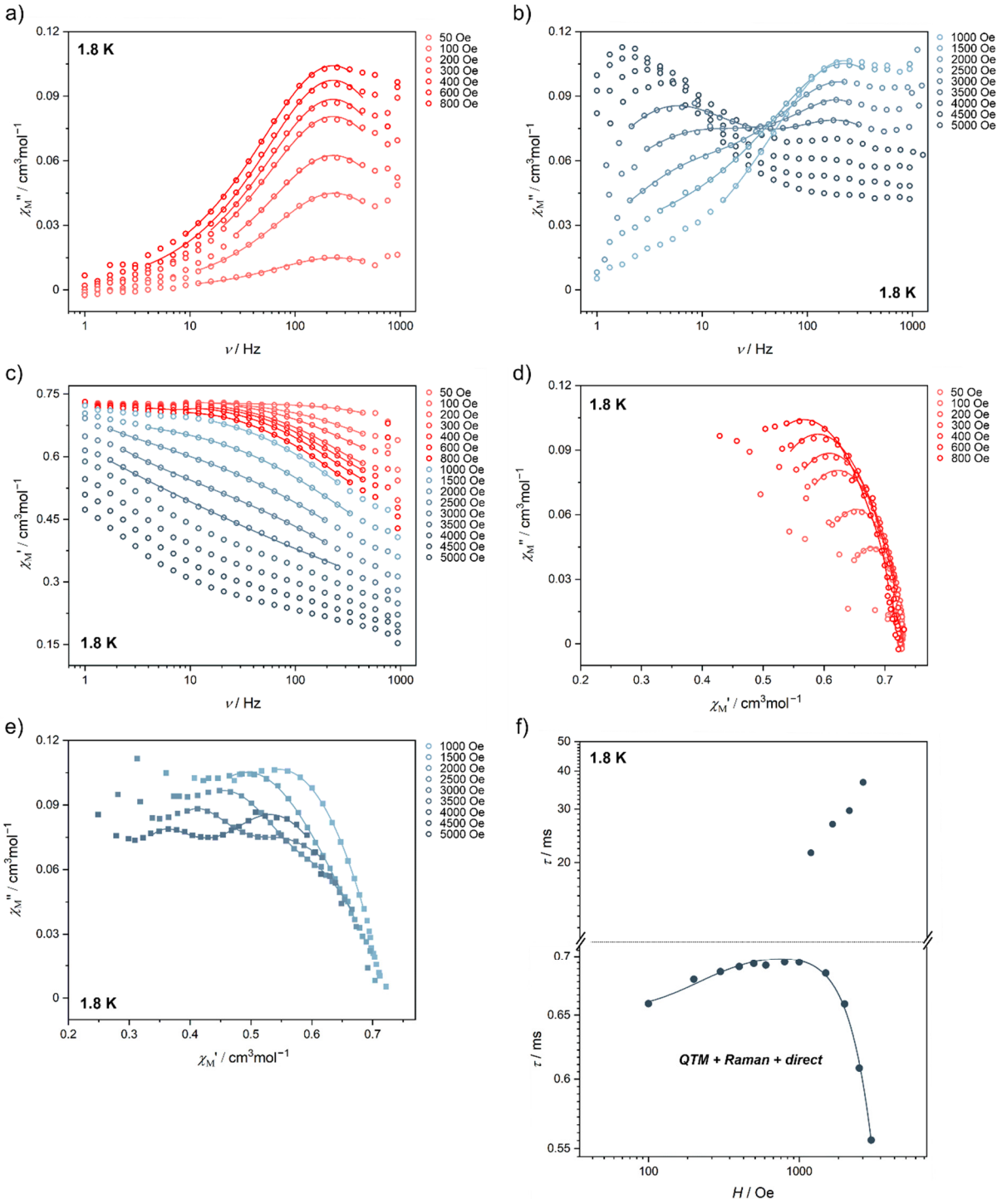


**Figure S23.** Magnetic–field–variable alternate–current (*ac*) magnetic characteristics of **1·MalCN** at $T$ = 1.8 K, and their analysis: the frequency dependences of the out-of-phase susceptibility, $\chi_M''$, under variable indicated *dc* fields (a, b), the frequency dependences of the in-phase susceptibility, $\chi_M'$, under indicated *dc* fields (c), the related Argand plots (d, e), and the field-dependence of relaxation time, $\tau$ for two analyzed relaxation processes (f). Colored solid curves in (a–e) represent the best-fits using the generalized Debye model for a single or a double relaxation processes (depending on the shape of *ac* curves, see comment to Figures S15–S24). Solid line in (f) show the best-fit taking into account QTM, a Raman process, and a direct process (Equation 1). Best-fit parameters are gathered in Table 1.

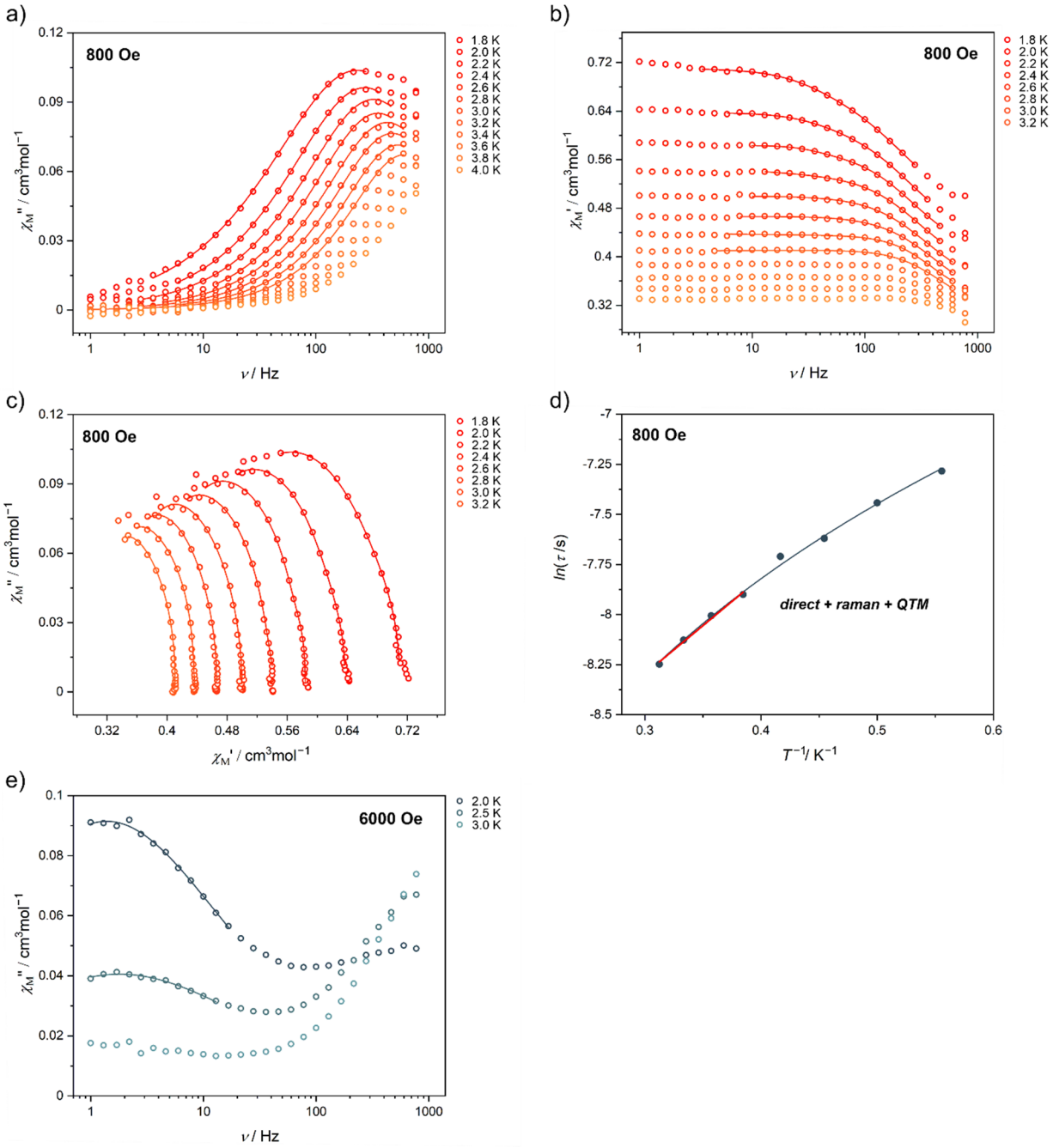


**Figure S24.** Temperature–variable alternate–current (*ac*) magnetic characteristics of **1·MalCN** under $H_{dc}$ of 800 Oe (a-d) or 6000 Oe (e), and their analysis: the frequency dependences of the out-of-phase susceptibility, $\chi_M''$, at various indicated temperatures under $H_{dc}$ = 800 Oe (a), the frequency dependences of the in-phase susceptibility, $\chi_M'$, at various indicated temperatures under $H_{dc}$ = 800 Oe (b), the related Argand plots (c), the temperature dependence of the resulting relaxation time, $\tau$ (d), and the frequency dependences of the $\chi_M''$ at various indicated temperatures under $H_{dc}$ = 6000 Oe (e). Colored solid curves in (a-c, e) represent the best-fits using the generalized Debye model for a single relaxation process. Solid blue line in (d) show the best-fit taking into account QTM, a Raman process, and a field-induced direct process (equation 1), while red line represents the linear fitting following the Arrhenius law for the limited temperature range of 2.6–3.2 K. Best-fit parameters are gathered in Table 1.

**Comment to Figures S15–S24**

For the fitting of the frequency dependences of $\chi_M'$ and $\chi_M''$ contributions to the *ac* magnetic susceptibility, and the related Argand $\chi_M''(\chi_M')$ plots (Figures S15–S24), the following equations representing a generalized Debye relaxation process model were applied:

$$\chi'(\omega) = \sum_i [\chi_{i,S} + (\chi_{i,T} - \chi_{i,S}) \frac{1+(\omega_i\tau_i)^{(1-\alpha_i)} \sin\left(\pi\alpha_i/2\right)}{1+2(\omega_i\tau_i)^{(1-\alpha_i)} \sin\left(\pi\alpha_i/2\right)+(\omega_i\tau_i)^{2(1-\alpha_i)}}]$$

$$\chi''(\omega) = \sum_i [(\chi_{i,T} - \chi_{i,S}) \frac{(\omega_i\tau_i)^{(1-\alpha_i)} \cos\left(\pi\alpha_i/2\right)}{1+2(\omega_i\tau_i)^{(1-\alpha_i)} \sin\left(\pi\alpha_i/2\right)+(\omega_i\tau_i)^{2(1-\alpha_i)}}]$$

where:

$\chi_S$ = the adiabatic susceptibility (at infinitely high frequency of *ac* field),

$\chi_T$ = the isothermal susceptibility (at infinitely low frequency of *ac* field),

$\tau$ = the relaxation time,

$\alpha$ = the distribution (Cole-Cole) parameter,

and $\omega$ is an angular frequency, that is $\omega = 2\pi\nu$, with ν being for the linear frequency in the [Hz] units [S16, S17].

For the fittings of magnetic–field–variable alternate–current (*ac*) magnetic susceptibility data the Debye model for a single (**1·MeCN@Lu**, **1·AcrCN** and **1·PrCN**; *i*=1) or a double (**1·MeCN** and **1·MalCN**; *i*=2) relaxation processes were applied. However for the temperature–variable alternate–current (*ac*) magnetic susceptibility, only the single relaxation process were applied. All related data are shown in Figures S15–S24.

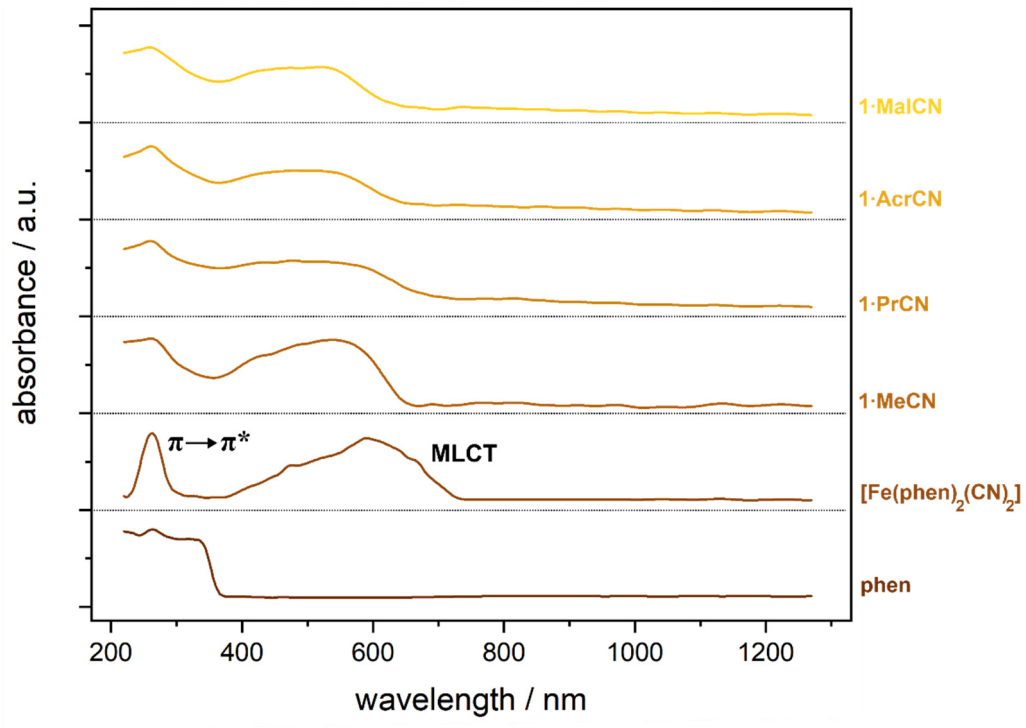


**Figure S25.** Solid-state UV-vis-NIR absorption spectra of **1·MeCN**, **1·PrCN**, **1·AcrCN**, and **1·MalCN** measured at room temperature in the 220–1350 nm range, and compared with the analogous absorption spectra of $[Fe^{II}(phen)_2(CN)_2]\cdot 2H_2O$ precursor and 1,10-phenantroline (phen) ligand.

**Comment to Figure S25:**

All compounds, **1·MeCN**, **1·PrCN**, **1·AcrCN**, and **1·MalCN**, exhibit strong absorption in the UV and visible range responsible for their deep red color. The spectra consist of two main parts, of which the strong band located at higher wavelengths (380–652 nm) corresponds to a charge transfer transition (MLCT) from $Fe^{II}$ centers to phen ligands. In comparison to the $[Fe(phen)_2(CN)_2]\cdot 2H_2O$, the CT band is shifted toward lower wavelengths. This is due to the coordination of the lone electron pair located on the nitrogen atom of the $CN^-$ ligand to $Yb^{3+}$ ions, which enhances the π–bonding interaction between $Fe^{2+}$ and $CN^-$, but weakens the interaction between $Fe^{2+}$ and the phen ligand [S18]. The second, higher energy band observed in the 220–280 nm UV range is related to the 1,10-phenantoline and/or 4-pyridne spin–allowed electronic transitions of the $\pi \rightarrow \pi^*$ character [S19].

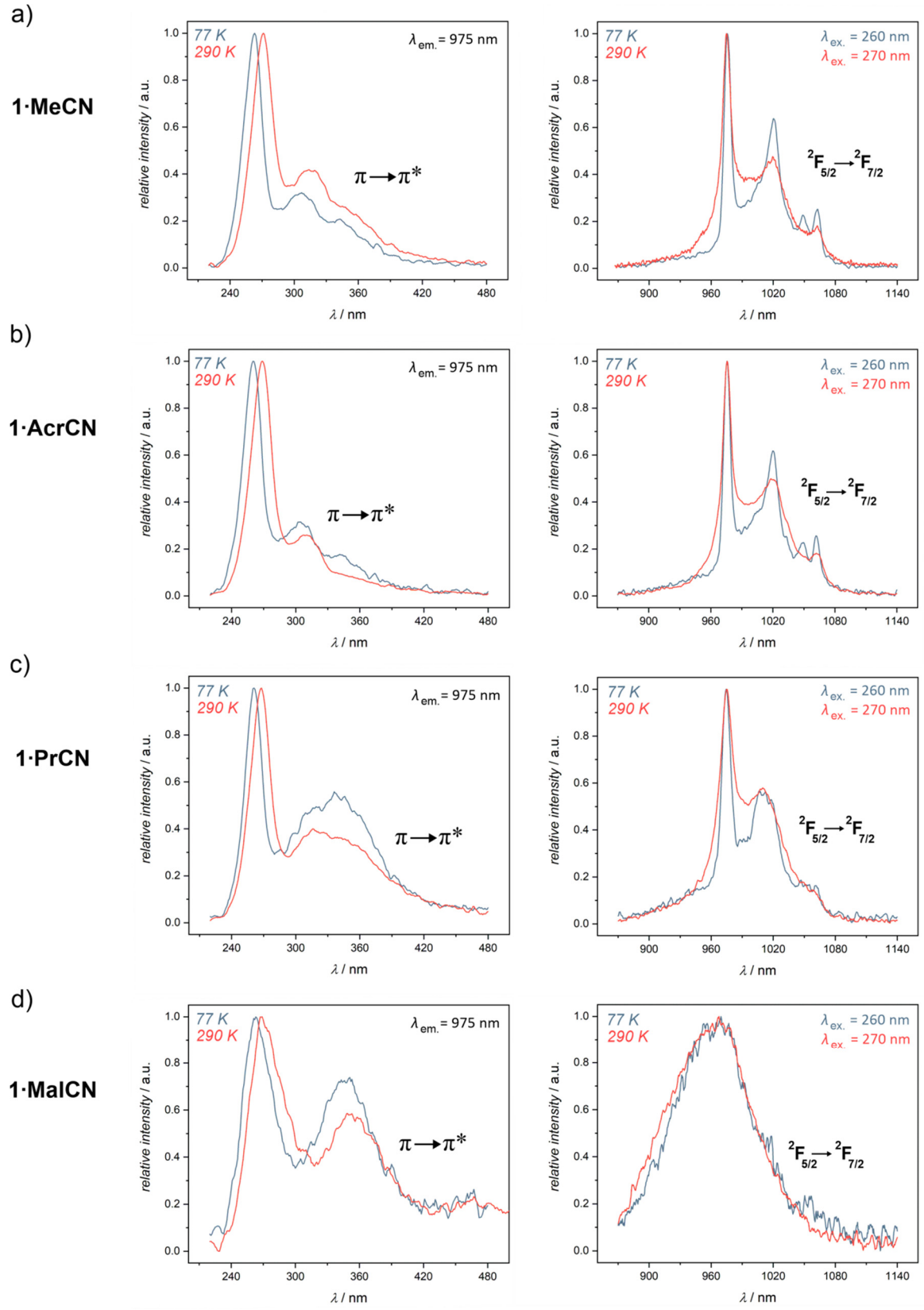


**Figure S26.** Solid–state excitation (left panel) and emission (right panel) spectra of **1·MeCN** (a), **1·PrCN** (b), **1·AcrCN** (c), and **1·MalCN** (d) gathered at 77 K and 290 K. Main electronic transitions responsible for the excitation ($\pi \rightarrow \pi^*$ transitions within the organic ligands) and for the emission signal (indicated f-f electron transitions of $Yb^{III}$) are indicated.

## References to Supporting Information:


1. Boumizane, K.; Herzog-Cance, M. H; Jones, D. J; Pascal, J. L.; Potier, J.; Roziere, J. Synthesis, vibrational spectroscopy and EXAFS analysis of some divalent and trivalent trifluoromethanesulphonato complexes. *Polyhedron* **1991**, *10*, 2757–2769.
2. Grochala, W.; Cyrański, M. K.; Derzsi, M.; Michałowski, T.; Malinowski, P. J.; Mazej, Z.; Kurzydłowski, D.; Koźmiński, W.; Budzianowski, A.; Leszczyński, P. J. Crystal and electronic structure, lattice dynamisc and thermal properties of Ag(I)($SO_3$)R (R = F, $CF_3$) Lewis acids in the solid state. *Dalton Trans.* **2011**, *41*, 2034–2047.
3. Schilt, A. A. Mixed Ligand Complexes of Iron(II) and (III) with Cyanide and Aromatic Di-imines. *J. Am. Chem. Soc.* **1960**, *82*, 3000–3005.
4. Egashira, K.; Yoshimura, Y.; Kanno, H.; Suzuki, Y. TG–DTA study on the lanthanoid trifluoromethanesulfonate complexes. *J. Therm. Anal. Cal.* **2003**, *71*, 501-508.
5. Hori, H.; Yokota, H. Efficient oxygen–induced decomposition of triphenylsulfonium trifluoro-methanesulfonate to fluoride ions in subcritical water. *J. Fluor. Chem.* **2015**, *178*, 1–5.
6. Llunell M.; Casanova, D.; Cirera, J.; Bofill, J.; Alemany, P.; Alvarez, S.; Pinsky, M.; Avnir, D. *SHAPE v. 2.1. Program for the Calculation of Continuous Shape Measures of Polygonal and Polyhedral Molecular Fragments*; University of Barcelona: Barcelona, Spain, 2013.
7. Casanova, D.; Cirera, J.; Llunell, M.; Alemany, P.; Avnir, D.; Alvarez, S. Minimal Distortion Pathways in Polyhedral Rearrangements. *J. Am. Chem. Soc.* **2004**, *126*, 1755–1763.
8. Galvam I. F.; Vacher, M.; Alavi, A.; Angeli, C.; Aquilante, F.; Autschbach, J.; Bao, J. J.; Bokarev, S. I.; Bogdanov, N. A.; Carlson, R. K.; et al. OpenMolcas: From Source Code to Insight. *J. Chem. Theory Comput*. **2019**, *15*, 5925–5964.
9. Roos B. O.; Lindh, R.; Malmqvist, P.-Å.; Veryazov, V.; Widmark, P.-O. Main group atoms and dimers studied with a new relativistic ANO basis set. *J. Phys. Chem. A* **2004**, *108*, 2851–2858.
10. Roos B. O.; Lindh, R.; Malmqvist, P.-Å.; Veryazov, V.; Widmark, P.-O. New relativistic ANO basis sets for transition metal atoms. *J. Phys. Chem. A* **2005**, *109*, 6575–6579.
11. Roos B. O.; Lindh, R.; Malmqvist, P.-Å.; Veryazov, V.; Widmark, P.-O.; Borin, A. C. New Relativistic Atomic Natural Orbital Basis Sets for Lanthanide Atoms with Applications to the Ce Diatom and $LuF_3$. *J. Phys. Chem. A* **2008**, *112*, 11431–11435.
12. Malmqvist, P. Å.; Roos, B. O.; Schimmelpfennig, B. The Restricted Active Space (RAS) State Interaction Approach with SpinOrbit Coupling. *Chem. Phys. Lett.* **2002**, *357*, 230−240.
13. Heß, B. A.; Marian, C. M.; Wahlgren, U.; Gropen, O. A Mean Field Spin-Orbit Method Applicable to Correlated Wavefunctions. *Chem. Phys. Lett.* **1996**, *251*, 365−371.
14. Chibotaru, L. F.; Ungur, L. Ab initio calculation of anisotropic magnetic properties of complexes. I. Unique definition of pseudospin Hamiltonians and their derivation. *J. Chem. Phys.* **2012**, *137*, 064112.
15. Ungur, L.; Chibotaru, L. F. Ab Initio Crystal Field for Lanthanides. *Chem. Eur. J.* **2017**, *23*, 3708–3718.
16. Guo, Y.-N.; Xu, G.-F.; Guo, Y.; Tang, J. Relaxation dynamics of dysprosium(III) single molecule magnets. *Dalton Trans.* **2011**, *40*, 9953–9963.
17. Ramos Silva, M.; Martin-Ramos, P.; Coutinho, J. T.; Pereira, L. C. J.; Martin-Gil, J. Effect of the capping ligand on luminescent erbium(III) β-diketonate single-ion magnets. *Dalton Trans.* **2014**, *43*, 6752–6761.
18. Tłaczała, T.; Bartecki, A. Studies on the solvatochromism of $Fe(CN)_2(phen)_2$. *Chemical Monthly* **1997**, *128*, 225–234.
19. Armaroli, N.; De Cola, L.; Balzani, V.; Sauvage, J.-P.; Dietrich-Buchecker, C. O.; Kern, J.-M.; Adsorption and luminescence properties of 1,10-phenanthroline, 2,9-diphenyl-1,10-phenanthroline, 2,9-dianisyl-1,10-phenanthroline and their protonated forms in dichloromethane solution. *J. Chem. Soc., Faraday Trans.* **1992**, *88*, 553–556.